AGU PUBLICATIONS

JGR

Journal of Geophysical Research: Solid Earth

RESEARCH ARTICLE
10.1002/2016JB013111

Key Points:
- Quantify the effect of rupture complexity on regional probabilistic tsunami hazard assessment
- Update the PTHA for the South China Sea using the best available seismic, geodetic, and tectonic data along the Manila megathrust
- Recommend appropriate patch size for Green's function approach to best balance the constraints of dispersion effect and others

Supporting Information:
- Supporting information S1

Correspondence to:
A. D. Switzer,
aswitzer@ntu.edu.sg

Citation:
Li, L., A. D. Switzer, C.-H. Chan, Y. Wang, R. Weiss, and Q. Qiu (2016), How heterogeneous coseismic slip affects regional probabilistic tsunami hazard assessment: A case study in the South China Sea, *J. Geophys. Res. Solid Earth*, *121*, 6250–6272, doi:10.1002/2016JB013111.

Received 20 APR 2016
Accepted 24 JUL 2016
Accepted article online 16 AUG 2016
Published online 30 AUG 2016

How heterogeneous coseismic slip affects regional probabilistic tsunami hazard assessment: A case study in the South China Sea

Linlin Li[1], Adam D. Switzer[1,2], Chung-Han Chan[1], Yu Wang[1], Robert Weiss[3], and Qiang Qiu[1,2]

[1]Earth Observatory of Singapore, Nanyang Technological University, Singapore, [2]Asian School of the Environment, Nanyang Technological University, Singapore, [3]Department of Geosciences, Virginia Tech, Blacksburg, Virginia, USA

Abstract Rupture complexity, typically in the form of heterogeneous slip distribution pattern, significantly affects the local tsunami wave field. However, the effect of rupture complexity is not commonly considered in any form of tsunami hazard assessment. Taking rupture complexity into account significantly increases the computational load, particularly in regional-scaled probabilistic tsunami hazard assessments (PTHAs) that usually require a large number of simulations based on synthetic scenarios. In this study, we investigate how the heterogeneous slip distribution affects the regional-scaled PTHA by taking the South China Sea (SCS) as an example. By doing this, we update PTHA for the SCS by incorporating the best available information of seismic tsunamigenic sources along the Manila megathrust. We integrate a stochastic source model into a Monte Carlo-type simulation, in which a broad range of slip distribution patterns is generated for large numbers of synthetic earthquake events. Green's function technique is employed to efficiently calculate the nearshore tsunami wave amplitude along the SCS coastlines. Our result suggests that for a relatively small and confined region like the SCS, the commonly used approach based on the uniform slip model significantly underestimates tsunami hazard not only in the near-source region like west Luzon, as expected, but also in the relative far field, such as south China and central Vietnam. Additionally, our sensitivity test of the patch size effects suggests that large patch size is unable to adequately resolve the details of heterogeneous seafloor deformation, and such approaches considerably underestimate the potential tsunami hazard for the SCS coasts.

1. Introduction

Rupture complexity, typically in the form of heterogeneous slip distribution on fault plane, significantly impacts the near-field tsunami wave field [*Geist*, 1998, 2002; *Geist and Dmowska*, 1999; *Løvholt et al*., 2012; *McCloskey et al*., 2007]. Earthquakes with similar rupture areas, fault geometries, and seismic moments, but with varying fault slip distributions, could generate significantly different tsunami wave heights. For example, *Geist's* [2002] numerical experiments along the coastline of Mexico show the peak nearshore tsunami amplitudes generated from 100 M_w 8.1 scenarios of random slip distribution could vary by a factor of 3 or more. A recent study also suggests the tsunami inundation extent, which is roughly proportional to the tsunami wave height, could be underestimated by an equivalent magnitude of 0.3 to 0.4 if fault slip is assumed to be uniform during the main shock (i.e., an M_w 8.7 to M_w 8.8 earthquake with uniform slip creates inundation area comparable to an M_w 8.4 one with nonuniform slip) [*Mueller et al*., 2015]. Although the significant effect of heterogeneous fault slip has been increasingly recognized, it is still not commonly considered in any forms of tsunami hazard assessment (i.e., deterministic scenario-based approach or probabilistic approach) [*Burbidge et al*., 2008; *Power et al*., 2013; *Sørensen et al*., 2012], even though the heterogeneous slip model could clearly yield more accurate assessments than the uniform slip-based methods [*Geist*, 2002; *Mueller et al*., 2015]. One of the primary reasons blocking the use of heterogeneous slip model is the limitation of computational power; a secondary reason include a general unawareness of the significance of the influences of rupture complexity.

This opens questions which have not been addressed before: to what extent does the rupture complexity affect probabilistic tsunami hazard assessment, and at what propagation distance does the effect of heterogeneous slip feature become insignificant? In this study, we answer such questions by integrating a stochastic source model into a Monte Carlo-type probabilistic tsunami hazard assessment (PTHA). Our work differs from previous studies addressing the effect of rupture complexity, which have so far been limited to the near

field with only one or few earthquake magnitudes considered [*Fukutani et al*., 2014; *Geist*, 2002; *Løvholt et al*., 2012; *McCloskey et al*., 2008; *McCloskey et al*., 2007; *Mueller et al*., 2015]. Here we investigate this effect in a much broader region, the South China Sea, and consider numerous earthquakes with a wide range of magnitudes. Such choice allows us to quantify the effect of rupture complexity on a regional basis when other factors like source directivity, bathymetry effect, or wave dispersion effect is also presented.

The South China Sea (SCS) is an ideal region for such a study for several reasons.

1. In some regions (e.g., the Pacific Ocean and the Indian Ocean), tsunami warning systems are already in place; some countries bordering these regions (e.g., the United States, Canada, and Japan) start taking tsunami hazard into account in building codes and tsunami planning. However, the coasts of the SCS are still rapidly developing their tsunami warning systems and remain far away from applying such hazard impact into practical preparedness and land use planning. The key reason behind such slowness of building tsunami warning systems is that the risk of large tsunamis in the SCS is commonly underestimated or unrecognized due to the sparse and less convincing historical tsunami records (Figure 1), although several PTHAs related to this region have highlighted the potential tsunami threat posed by the Manila megathrust [*Liu et al*., 2007; *Ren et al*., 2014; *Thio et al*., 2007]. In this study, we improve previous PTHAs based on the best available seismic, geodetic, and geophysical data. Our assessment serves as a reference for future studies in this region.
2. Previous tsunami hazard assessments of this region could be improved by considering the effect of rupture complexity or by better constraining fault geometry. For example, most of the previous fault models used in either deterministic tsunami hazard analyses or PTHAs assume uniform slip along the dip direction [*Dao et al*., 2009; *Liu et al*., 2007; *Megawati et al*., 2009; *Okal et al*., 2011; *Ren et al*., 2014; *Thio et al*., 2007; *Wu and Huang*, 2009]. This assumption likely underestimates the potential tsunami hazard [*Geist*, 2002; *Mueller et al*., 2015].
3. The relatively enclosed geographical setting of the SCS allows us to consider only tsunamigenic sources inside the sea (i.e., the Manila megathrust), avoiding the complexity of inducing multiple tsunamigenic faults. Well-sheltered by the Luzon Trench in the east and the Sunda Arc in the south, the coasts of the SCS would be only minimally affected by tsunamis outside the sea, as demonstrated by the two recent largest tsunamis, the 2004 Indian Ocean Tsunami and the 2011 Tohoku Tsunami, and supported by previous numerical modeling [*Okal et al*., 2011].

In this paper, we first define the study area and the tsunamigenic source parameters. We then explain our understanding of the seismogenic behavior of the Manila subduction zone based on the best available data. This is followed by the key elements of our PTHA, which includes the mechanism of the stochastic source model, fault parameters, and the tsunami modeling process. Next, we show the hazard assessment results in the form of hazard curves and maps. Then we compare the hazard assessment result given by nonuniform slip models with the one given by traditionally used uniform slip models. By quantifying the differences between the two sets of results, we address the question of how significant the effect of slip variations is, for the medium field and relatively far field. In addition, we dig deeper to explain why the nonuniform and uniform slip model results differ. In particular, for the Monte Carlo-based PTHA we applied in this study, we further examine the number of earthquakes that is adequate to capture the natural variability of the potential tsunami wave height range. We also investigate how the patch size chosen for the Green's function affects the hazard assessment result and recommend an appropriate patch size which could approximate the slip pattern, avoid wave dispersion effect, and balance the computational load at the same time. We conclude by summarizing our findings.

2. The Manila Trench

Our case study is confined to the coastlines bordering the SCS. Coastlines that could be affected by earthquakes originating from sources outside the SCS are not included in this work. Such uncounted coastlines include the Philippines' east coast, which could be affected by the Pacific Rim tsunamigenic earthquakes or the regions bordering the Sulu Sea and Celebes Sea, which could be affected by local subduction events inside the seas (Figure 1). Given this spatial delineation, the only tsunamigenic source we consider is the megathrust along the Manila Trench, which is thought to be capable of producing basin-wide tsunamis as demonstrated by deterministic tsunami models, and thus poses the greatest tsunami threat to the bordering

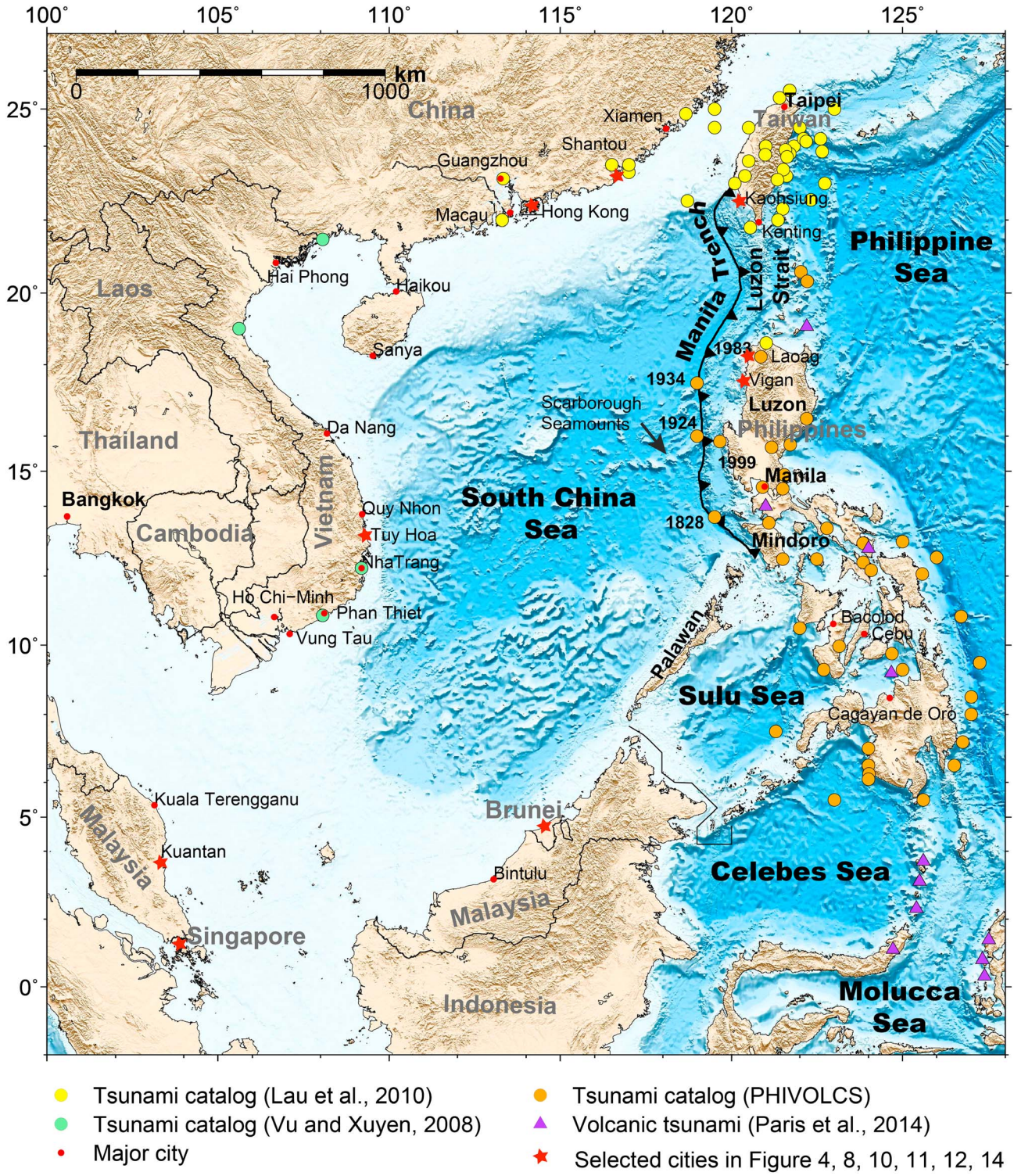

Figure 1. Locations of historical tsunamigenic earthquakes or tsunami affected areas in the SCS. Current available data show that both the Philippines and China were more frequently affected by tsunamis historically. Major cities are marked in red dots. The main tsunami threat in the SCS comes from the Manila Trench megathrust, along which no earthquake larger than M_w 7.8 has been observed since 1560s.

Table 1. Earthquake Return Period in Two Synthetic Earthquake Catalogs

	Catalog-SB			Catalog-GB		
	Zone I	Zone II	Zone III	Zone I	Zone II	Zone III
	$a = 5.97$	$a = 4.96$	$a = 6.20$	$a = 5.45$	$a = 5.74$	$a = 5.96$
M_w	$b = 1.20$	$b = 0.94$	$b = 1.12$	$b = 1.0$	$b = 1.0$	$b = 1.0$
7.0	467	93	80	75	39	23
7.2	810	143	133	120	61	37
7.4	1406	220	223	190	97	58
7.6	2441	338	372	300	154	93
7.8	4238	521	623	476	244	147
8.0	7357	802	1042	755	387	232
8.2	12772	1235	1743	1196	614	368
8.4	22172	1901	2915	1895	973	584
8.6			4876			925
8.8			8157			1466
9.0			13644			2324

coastlines [*Liu et al*., 2009; *Megawati et al*., 2009; *Wu and Huang*, 2009]. Local faults (e.g., littoral faults in the northeastern South China Sea and splay faults in the southwest offshore Taiwan) are not included for the following two reasons: (1) stable statistical models describing the frequency of earthquakes from these faults are currently not available and (2) the tsunami potential is constrained by either their spatial scale or fault type, therefore limiting the likely tsunami hazard [*Cao et al*., 2014; *Li et al*., 2015; *Ren et al*., 2014]. While other sources including landslides or volcanic eruptions could also generate devastating tsunamis as reported in the published literature [*Lau et al*., 2010; *Li et al*., 2015; *Paris et al*., 2014], the available historical records do not contain enough events to determine the source parameters and recurrence rate; therefore, such sources are also excluded. However, as demonstrated in a recent probabilistic landslide-tsunami hazard assessment for submarine canyons in central New Zealand [*Mueller et al*., 2016], the probabilities of the excluded sources could be considered in a future study when more information is available in this region, such as spatial landslide distribution or dates of the previous landslide events.

The Manila megathrust is the plate boundary fault between the Philippine Sea Plate and the Sunda/Eurasian Plate (Figure 1). Due to very limited observation time span and spatial coverage of seismic and geodetic data, the long-term seismogenic behavior of the Manila subduction zone remains poorly understood [*Hsu et al*., 2012; *Wang and Bilek*, 2014]. The estimated convergence rate varies along this ~1200 km long megathrust and systemically decreases southward from nearly 90 mm/yr at northern Luzon to 55 mm/yr north of Mindoro [*Hsu et al*., 2012]. Although the Manila megathrust is one of the fastest-moving megathrusts on Earth, and its convergent rate is comparable to other well-known giant-earthquake generating megathrusts (e.g., Japan, Alaska, Sunda, and northern Chilean megathrust [*McCaffrey*, 2008]), neither the instrumental earthquake records nor the multicentury-long historical earthquake catalog shows an event exceeding M_w 7.8 since 1560 Common Era [*Bautista et al*., 2013]. The conflicting information leads to two contrasting hypotheses that either the Manila megathrust predominantly slips aseismically or the megathrust was experiencing a long interseismic period before generating a series of giant earthquakes (e.g., Sunda megathrust) [*Sieh et al*., 2008]. These two possibilities serve as our motive for constructing two different synthetic earthquake catalogs.

We use both the global seismic catalog and the recent geodetic megathrust coupling analyses of the Manila megathrust to construct two 100,000 year long synthetic earthquake catalogs, following the assumption of truncated Gutenberg-Richter earthquake relationship (truncated G-R law in accumulated form). Table 1 shows the *a* and *b* values of the two synthetic catalogs and the discrete return periods for different magnitude spans. The seismic catalog we utilize is the U.S. Geological Survey's global earthquake catalog from 1973 to 2014 (the USGS/National Earthquake Information Center (NEIC) catalog), as the harmonized local earthquake catalog from the Philippines to Taiwan is not set up yet. The geodesy-based synthetic catalog is generated largely from the first-order GPS-based megathrust coupling model from *Hsu et al*. [2012] and using the approach suggested by *Ader et al*. [2012] and the truncated G-R relationship. As both the plate

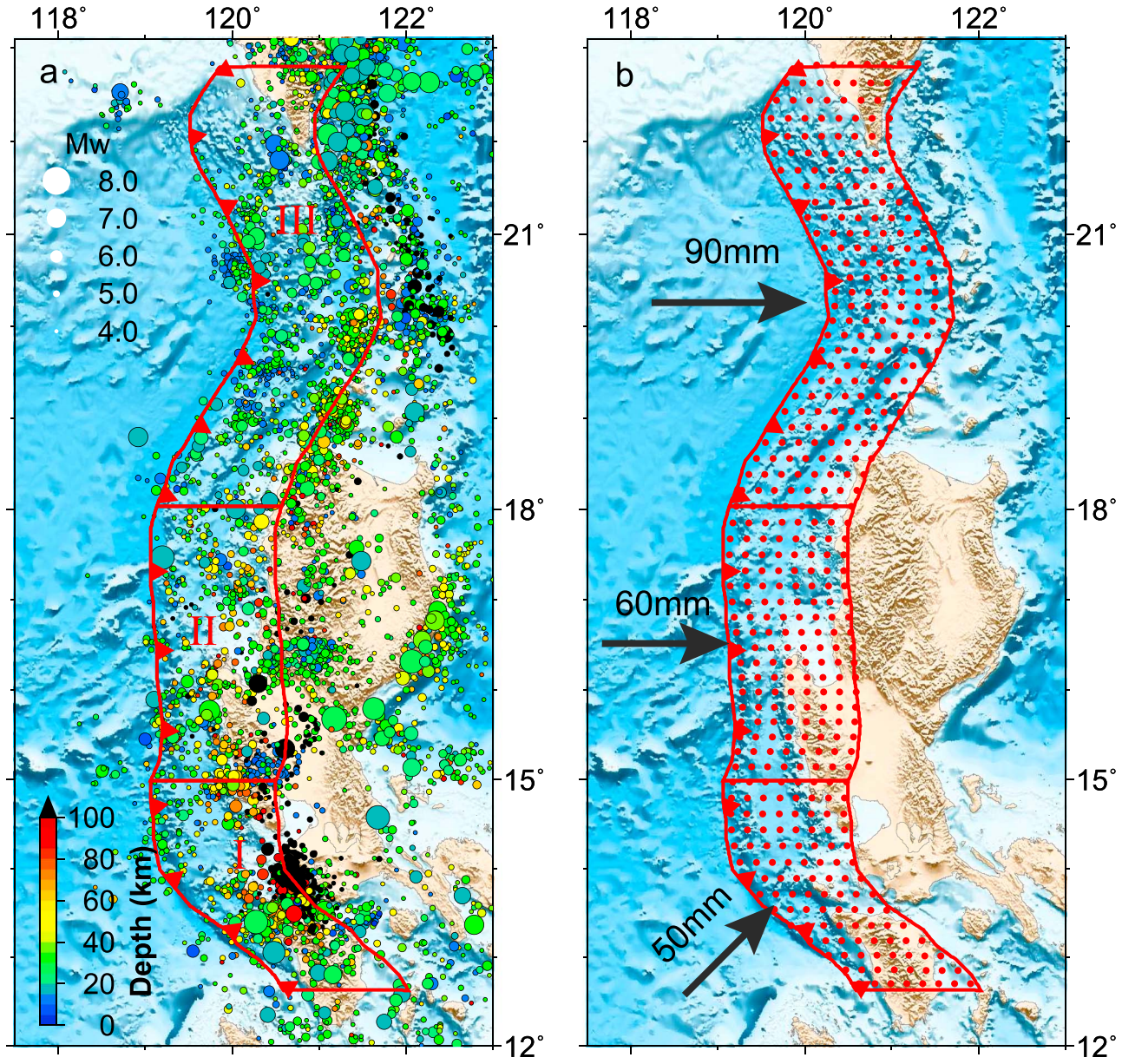

Figure 2. (a) Seismicity between 1973 and 2014 from NEIC (the U.S. Geological Survey National Earthquake Information Centre) and three zonation divided by Scarborough Seamount chain wherein oceanic floor is highly fractured; (b) the Manila subduction zone is divided into approximately 20 × 20 km patches (60 along the strike direction and 8 along the dip direction). Red dots show the center location of each patch. The convergence rates and coupling rates for these three zones are 50 mm and 0.2 for zone I, 60 mm and 0.25 for zone II, and 90 mm and 0.3 for zone III.

convergence rate across the Manila megathrust and the average megathrust coupling ratio change from north to south along the megathrust [*Hsu et al.*, 2012], we further separate the entire megathrust to three different zones (zones I, II, and III, see Figure 2) in both geodesy- and seismicity-based models, to better capture the convergence rate and seismicity rate at different parts of the megathrust fault (Figure 2a). The boundaries of these three zones are informed by the presence of the Scarborough seamount chain between latitudes 15 and 18°N, where the oceanic floor is highly fractured. We assume that the maximum magnitudes of earthquakes in each zone are constrained by the length and width of that zone and are M_w 8.4, M_w 8.4, and M_w 9.0 for zones I, II, and III, respectively. The three-zone model we used in this study does not include large earthquakes that could rupture through the rugged seamounts in zone II, which is the less likely scenario suggested by several previous studies [e.g., *Hsu et al.*, 2012; *Wang and Bilek*, 2014].

Comparing the seismicity-based and the geodesy-based G-R relationships of the Manila megathrust, we found both of them share similar b values ($b = 0.94$–1.20 and $b = 1$) throughout the defined area above the Manila megathrust, while the a values from the geodesy-based model ($a = 5.45$–5.97) is generally 3–4 times higher than the a values from the seismicity-based model ($a = 4.96$–6.20). While the geodesy-based model is only based on the first-order on-land GPS velocity field analysis, this difference does support the hypothesis that the Manila megathrust is still accumulating slip potency despite its average low coupling ratio (0.2 to 0.5) [*Hsu et al*., 2012, 2015]. To balance the estimates from these two different aspects, and to prevent the overestimation of the tsunami hazard, we then use the seismicity-based model as the lower bound and the geodesy-based model as the higher bound in our simulations. We discuss both their outcomes in the later part of this paper.

3. Modeling Framework

We apply a Monte Carlo technique in our PTHA in the SCS. For each geodesy- and seismicity-based synthetic catalog, we derive two sets of PTHA results: one is produced by a commonly used uniform slip source model, and the other one is produced by the heterogeneous slip model, which is in turn generated by a stochastic source model. For each tsunamigenic earthquake event with the magnitude larger than 7.0 in the synthetic catalogs, we simulate tsunami propagation scenarios, and record the peak nearshore tsunami amplitude (PNTA) at predefined forecasting locations. The simulation results from all the scenarios are then aggregated at these locations to determine their hazard level. In total, nearly 30,000 synthetic earthquakes with M_w between 7.0 and 9.0 are simulated. For the earthquake numbers of different magnitude spans in the two synthetic catalogs, please refer to supporting information Table S1.

3.1. Stochastic Source Model

Studies in the seismological research field [e.g., *Gallovič and Brokešová*, 2004a, 2004b; *Hartzell and Heaton*, 1983; *Herrero and Bernard*, 1994; *Somerville et al*., 1999] have proposed heterogeneous dislocation models to illustrate rupture behaviors for earthquakes. Such models describe coseismic dislocation spatially using finite-fault models, which can be obtained through inversion from seismological, geodetic, or/and geological observations. In most real cases, the dislocation focuses on one or more asperities, rather than uniform slip on fault plane, especially for large earthquakes. For example, whereas the 2004 Sumatra earthquake is attributed to the rupture length of more than 1000 km, its maximum slip asperity takes place at the southern segment of the rupture [*Ammon et al*., 2005; *Rhie et al*., 2007]. The downdip width of the 2011 Tohoku earthquake was ~500 km, but the coseismic slip was focused in the shallow part of the megathrust, which resulted in the devastating tsunami [*Satake et al*., 2013]. These examples underscore the importance of a heterogeneous slip model for tsunami hazard assessment.

To present the earthquake behavior of slip asperity, we propose models that incorporate spatial heterogeneous slip patches on a plane. The heterogeneous slip is generated by a hybrid kinematic k-squared source model proposed by *Gallovič and Brokešová* [2007] (access the code in this link http://fgallovic.github.io/SlipGen/). We assume the fault with dimensions $L \times W$. Assuming that the subfault dimension is $L_{sub} \times W_{sub}$, the number of subfaults is $L/L_{sub} \times W/W_{sub}$. The slip on each subfault is assigned randomly but follows the self-similar regularity proposed by *Herrero and Bernard* [1994], where the sum of the moment from all the subfaults corresponds to the seismic moment of the earthquake.

To validate whether this stochastic source model is capable of providing realistic fault models to represent the real case, we take the 2011 Tohoku earthquake and tsunami as an example. We use the tsunami wave height generated by rupture model proposed by *Yue and Lay* [2013] as benchmarks to justify if a certain number of synthetic fault models could also produce a reasonable range of tsunami wave height with the benchmark height included. *Yue and Lay's* [2013] model is chosen because this model could reproduce the waveform recorded by tide gauge and Deep-ocean Assessment and Reporting of Tsunamis well. We simulate 100 synthetic scenarios, each with different slip distributions but following the same geometry and magnitude with *Yue and Lay's* [2013] model. The peak nearshore tsunami amplitudes at 34 synthetic gauges are derived from these 100 scenarios and the real case scenario (see comparison in Figure S1). As shown in Figure S1, the wave height ranges produced by the synthetic scenarios cover most of the wave heights given by *Yue and Lay's* [2013] model, which validated that this stochastic source model is able to capture the real tsunami wave height when a sufficient number of synthetic scenarios are simulated.

Table 2. Rupture Dimension Determined by Two Scaling Relationships

	Length(km)	Width (km)	Length(km)	Width (km)			
M_w	*Papazachos et al.* [2004]		*Blaser et al.* [2010]		Selected Locations	*W*	Slip Value (m)
7	45.7	34.7	41.7	22.9	40	40	0.82
7.2	58.9	40.0	54.2	28.3	60	40	1.09
7.4	75.9	46.1	70.5	35.0	80	40	1.63
7.6	97.7	53.2	91.6	43.3	100	40	2.61
7.8	125.9	61.4	119.1	53.5	120	60	2.89
8	162.2	70.8	154.9	66.1	160	80	3.24
8.2	208.9	81.7	201.4	81.7	200	80	5.17
8.4	269.2	94.2	261.8	100.9	300	100	5.51
8.6	346.7	108.6	340.4	124.7	400	120	6.87
8.8	446.7	125.3	442.6	154.2	440	140	10.67
9	575.4	144.5	575.4	190.5	560	160	14.64

3.2. Fault Parameters

The fault geometry used in this study follows that constructed by *Hsu et al*. [2012], which is based on earthquake focal mechanisms and the curvature of the Manila Trench (Figure 2). The dip angle of this geometry varies from 10 to 20° at shallow depths to around 30° at depths larger than 30 km in offshore northern Luzon. In the southern portion of this geometry, the dip angle steepens from 10° in zone II to 30° in zone III at depths shallower than 50 km at latitude 15°N. The three-dimensional fault geometry has a dimension of 1200 km in length with the width ranging from 160 km in the north to 100 km in the south. The widths are constrained by limiting the rupture depth to shallower than 50 km, which covers over 95% of the thrust-type events capable of generating appreciable tsunami waves.

For each synthetic earthquake with a given magnitude, its rupture length, width, and overall uniform slip are calculated by scaling relations (see formulas in supporting information Text S1) specially proposed for subduction zone events [*Blaser et al*., 2010; *Papazachos et al*., 2004] and approximated to values which are multiples of 20 km. The rupture area contains a specified number of patches in the strike direction and dip direction. For example, a M_w 7.0 earthquake has two patches in the strike direction and two in the dip direction, a M_w 8.4 earthquake has 15 and 5 in the strike and dip direction, respectively (see Table 2 for details). With the sequentially numbered patches, we group the patch numbers for each earthquake magnitude based on the required number of patches and then number the groups. The locations of the rupture area are randomly selected from the group numbers with the assumption that each area has equal rupture possibility. For the uniform slip distribution, an identical slip value is specified for each patch. For the non-uniform slip distribution, we first use the hybrid model [*Gallovič and Brokešová*, 2007] to generate high-resolution heterogeneous slip distributions in a rectangular area (the length and width of the area are equal to the rupture area calculated by scaling relations for each earthquake magnitude) and then project the generated slip distribution to the chosen rupture area with coarser patch sizes by averaging the high-resolution slip distribution and scaling the slip value to match the total overall slip imposed by the given moment magnitude. Figure 3 gives examples of slip distributions of M_w 8.0 earthquake produced by the aforementioned method. Using this method, varied slip distribution patterns can be generated for each randomly chosen rupture area.

3.3. Green's Function and Tsunami Simulation

Tsunami waveforms at nearshore locations of interest are obtained by adopting the Green's function concept [*Johnson and Satake*, 1994; *Satake*, 1987, 1989]. The underlying principle of this concept is that the linear behavior of tsunami waves is valid during the wave propagation from deep sea to a certain water depth offshore. Under this principle, the fault area could be divided into a set of subfaults. Each subfault with unit slip is treated as one source to generate a tsunami. The waveform at each specified offshore location can then be calculated through a linear superposition of the waveform generated by each subfault. Following this approach, we decompose the Manila megathrust into 480 subfaults, with 60 positioned along the strike and 8 along the dip direction. The average size of each subfault is 20 km × 20 km (Figure 2b). We use COMCOT (Cornell Multigrid Coupled Tsunami Model) [*Liu et al*., 1998] for tsunami simulation, which includes

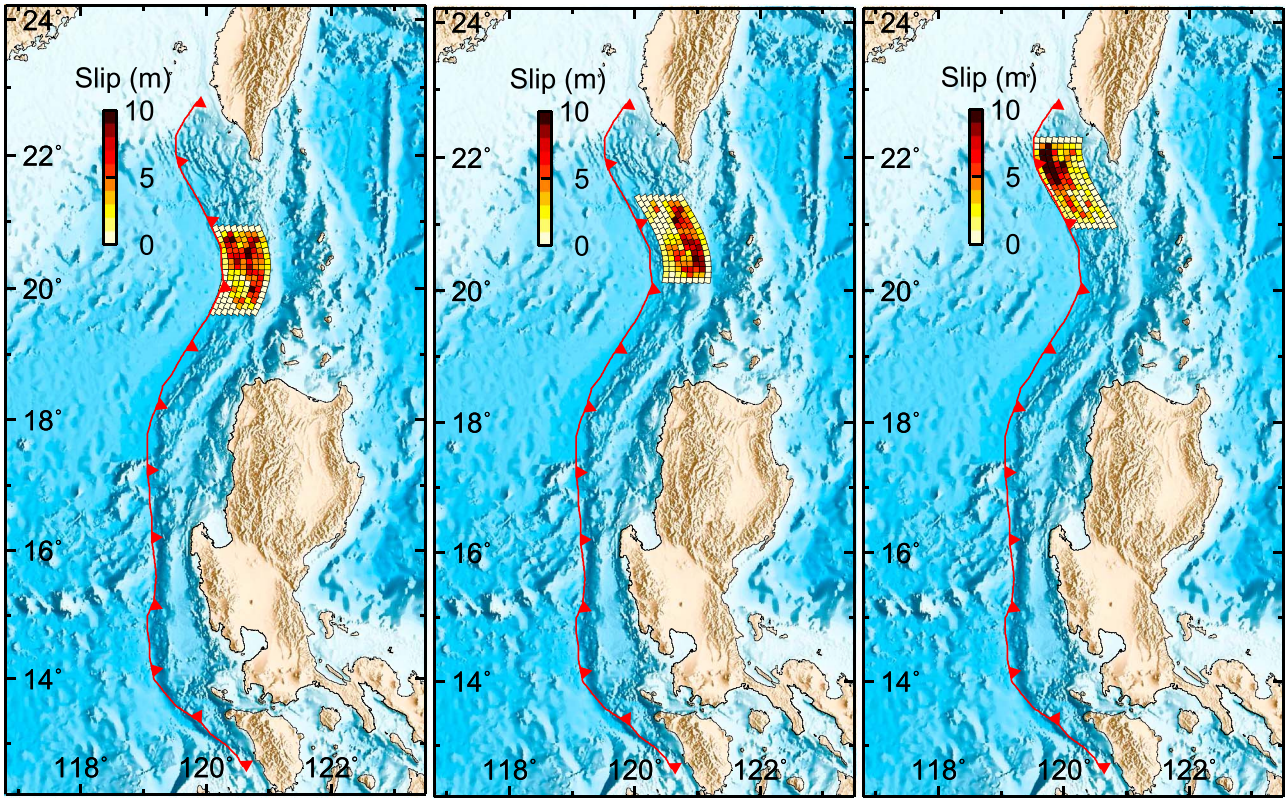

Figure 3. Examples of slip distributions of M_w 8.0 earthquake. The slip distributions are first generated by the hybrid model [*Gallovič and Brokešová*, 2007] in a rectangular area (the length and width of the area are equal to the rupture area calculated by scaling relations for each earthquake magnitude) and then projected to the chosen rupture area.

the process of wave generation (by Okada's [1985] model) and propagation from source to the coast. The simulation solves linear shallow water equations in Spherical coordinates (Coriolis force is considered) [*Wang*, 2009] over a 1 arc min bathymetric grid derived from the 30 arc sec General Bathymetric Chart of the Oceans (GEBCO) data (The GEBCO_08 Grid, available at http://www.gebco.net, accessed in October 2014). We apply one-layer grid in this study since we only solve linear shallow water equations in the deeper sea (>10 m). Using one-layer linear shallow water equation to simulate tsunami propagation in deeper sea is a widely accepted approach as long as the linear assumption is valid. As inundation is not included in the simulation, thus, wave breaking process and bottom friction are not considered. The time step used in the simulations is 4 s, which gives Courant-Friedrichs-Lewy (CFL) ranges between 0.02 and 0.46 suggesting that the simulations satisfy the CFL stability criterion. We then select 256 synthetic wave gauges (SWG) along 10 m isobath as the receivers to store tsunami waveforms. The linear assumption still holds at 10 m isobaths due to the relative narrowness of shallow water region in the SCS which has been verified by *Liu et al*. [2007] and the authors of this paper. With the waveform database at SWG, for any earthquake in the synthetic catalog with specific slip distribution, we can efficiently calculate tsunami waveforms at those SWG by summing the individual subfault waveforms scaled by their slip value. Such calculation approach applies to both uniform slip models and nonuniform slip models. The only difference is that the slip values of nonuniform models are generated in the way described in section 3.2, while the slip values of uniform model is identical for each patch. From the waveform at each SWG, we get the peak nearshore tsunami amplitude (PNTA). With the PNTAs of all the tsunami scenarios, we then construct a hazard curve for each SWG by calculating the frequency with which predefined tsunami amplitude thresholds are exceeded. Readers should note that the real runups could be several times higher than the corresponding PNTAs due to shoaling effects which are largely determined by the local bathymetry and topography. More accurate runup predictions and inundation areas can only be achieved through detailed inundation simulations with nested grids of finer resolution.

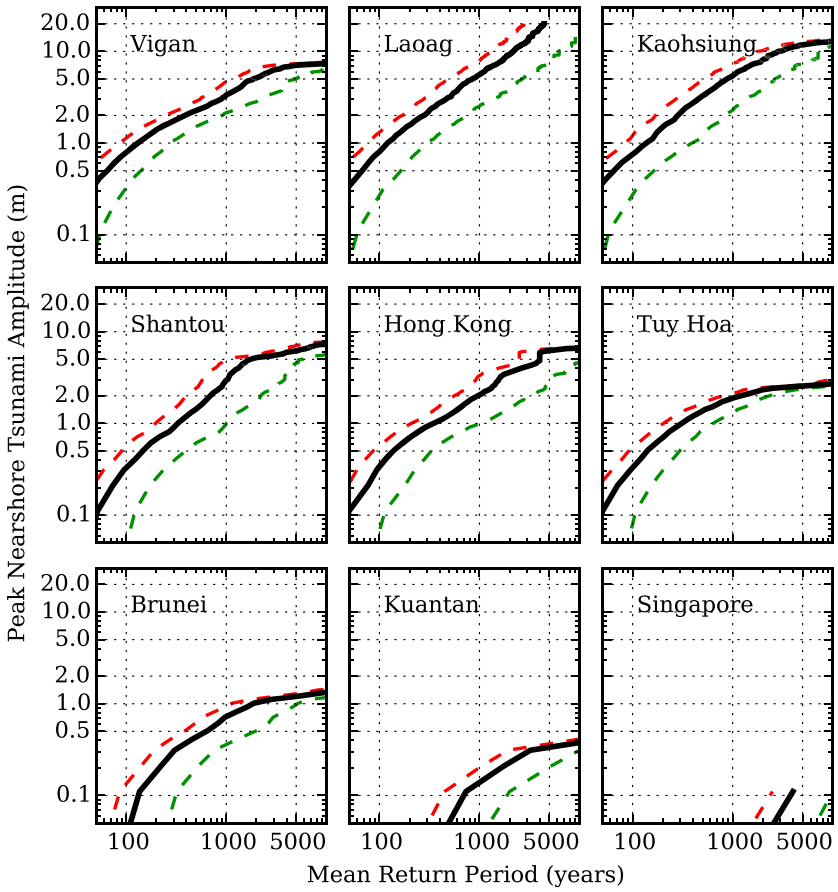

Figure 4. Hazard curves of nine selected locations show expected peak nearshore tsunami amplitude as a function of return period. Red dashed lines are hazard curves based on catalog-GB, and green dashed lines based on catalog-SB. Thick black lines are integrated result by giving the aforementioned results each a weighting factor of 0.5.

4. Hazard Assessment Results Based On Nonuniform Slip Models

4.1. Hazard Curves

Figure 4 shows the hazard curves (i.e., exceeding height of offshore tsunami as a function of return period) for nine selected locations in the South China Sea (see the locations in Figure 1, shown in red stars). Hazard curves derived from seismicity-based catalog (catalog-SB) and geodesy-based catalog (catalog-GB) vary greatly at all the locations examined. As expected from the much shorter return period in geodesy-based catalog, for the same return period, catalog-GB in general gives 2–4 times higher expected tsunami waves than the ones predicted by catalog-SB. For a 100 year return period, catalog-GB suggests we can expect tsunami waves larger than 1 m in the near-source region, represented by Vigan, Laoag, and KaoHsiung, and larger than 0.5 m in Shantou, Hong Kong, and Tuy Hoa, while catalog-SB predicts less than 0.3 m waves even for the near-source locations. Similarly, for a 1000 year return period, catalog-GB predicts tsunami waves greater than 5 m, with the maximum around 8 m in the near-source region, while catalog-SB gives less than a 3 m maximum wave height, which is significantly smaller. Results based on these two catalogs likely represent two extreme possibilities which provide upper bound and lower bound of the hazard level. The uncertainty for the return period analysis is due to our limited knowledge of tectonic setting and plate movement. This will likely be reduced when more data (GPS data, seismicity, etc.) is collected in the future. To incorporate such epistemic uncertainty into probabilistic calculations, we employ a logic tree to integrate the two sets of results by giving each a weighting factor of 0.5, assuming therefore that each has a 50% chance of being correct [*Annaka et al.*, 2007]. All the results we present in this paper are the integration of the results predicted by catalog-SB and catalog-GB.

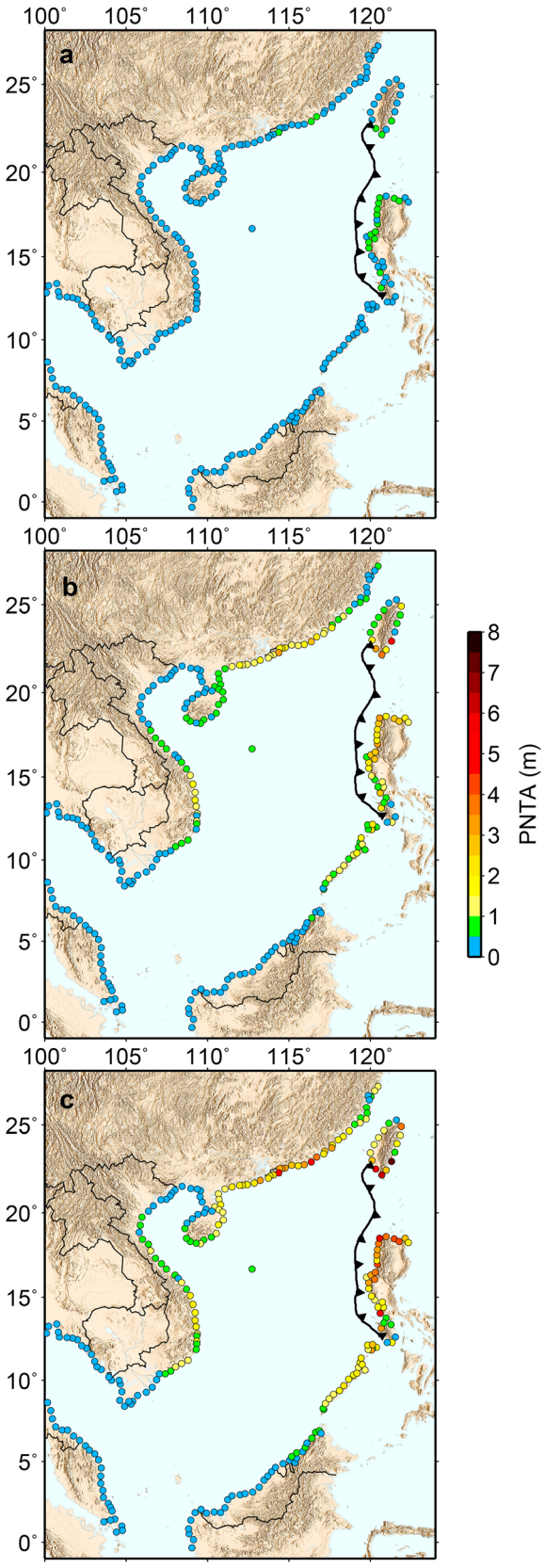

Figure 5. Probabilistic hazard maps show expected PNTAs with return periods of (a) 100 years, (b) 500 years, and (c) 1000 years.

4.2. Hazard Maps

Figure 5 shows PNTA with different return periods from our weighted model results. For any given return period, the near-source regions including western Luzon and southern Taiwan face the greatest tsunami hazard. The second most threatened area is southern China, followed by eastern Vietnam and western Palawan. Significantly less affected areas are coastal regions of northern Borneo, eastern Malaysia, eastern Thailand, and southern Cambodia.

At the relatively short time scale of a 100-year return period, only locations in west Luzon, southwest Taiwan, and southern China could expect 0.5–1.0 m tsunami waves. However, the expected wave height and the length of affected coastline increase dramatically with the increase of return period. For a 500 year return period, western Luzon and southern Taiwan can expect 2–4 m tsunami waves, with 1–3 m for southern China, and 0.5–2 m for eastern Vietnam and western Palawan. At a 1000 year return period, the expected maximum wave height reaches 7–8 m in western Luzon and southern Taiwan, $>$ 4 m in southern China, and 2–3 m in eastern Vietnam and western Palawan. The estimated hazard level in the 100 year return period actually matches the historical observation in northwest Luzon, where most coastlines have experienced ~1 m tsunami waves once during five confirmed earthquake events, namely, the November 1828, May 1924, February 1934, August 1983, and December 1999 earthquakes (see the earthquakes' locations in Figure 1) [*Bautista et al.*, 2013]. Hazard levels can also be presented in terms of the probability of exceeding a given PNTA in a fixed time period (see Figure S2 for the probability of a tsunami wave exceeding 1 m and 2 m in the next 100 years).

4.3. What Drives Wave Height Variability?

The variability of calculated tsunami wave heights in examined offshore locations is caused by many factors.

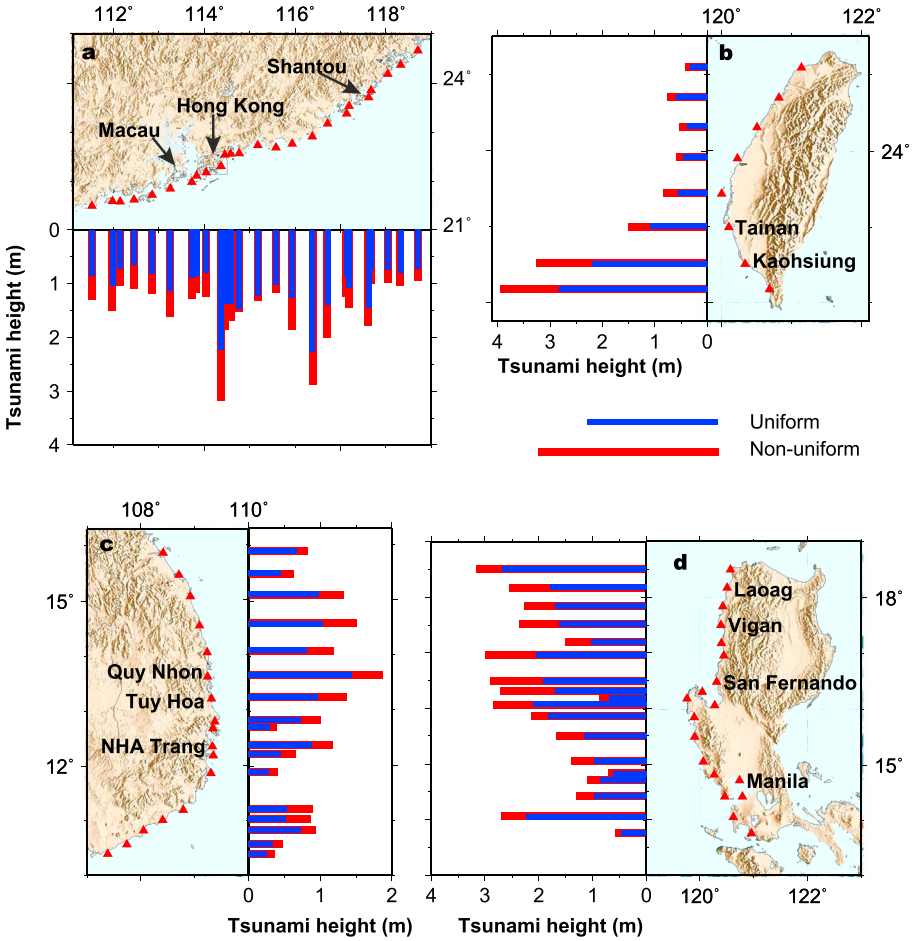

Figure 6. Comparison of expected peak nearshore tsunami amplitude (PNTA) with 500 year average return period given by approaches based on uniform slip fault model (blue bars) and nonuniform slip fault model (red bars) in (a) southeast China, (b) western Taiwan, (c) central Vietnam, and (d) western Luzon.

For each individual scenario we simulated in our synthetic catalog, directivity effects and bathymetry effects clearly play an important role in the resulting wave height of each receiving coastline. For example, the combined effect of directivity and bathymetry explains the abnormally high hazard along the southern Chinese coast. Tsunami waves originating from any portion of the Manila Trench refract significantly due to the shape and gradient of the continental slope, leaving southern China (including coastlines of Guangdong, Hong Kong, and Macau) in the direct tsunami path. Notably, the refraction phenomena are surprisingly dramatic for tsunamis generated from those rupture portions, because the azimuths of tsunamis would otherwise obviously not direct them toward southern China, as also noted by *Li et al*. [2015]. The directivity effect is also clearly demonstrated by the unexpectedly comparable hazard level between western Palawan and eastern Vietnam. Despite its proximity to the Manila Trench, western Palawan has the same tsunami hazard level as eastern Vietnam, which is 1000 km away from the source region. The fundamental difference between scenario-based tsunami hazard assessment and PTHA is the latter integrates information of source occurrence, in our case, earthquake frequency. The earthquake frequency in each zone is another controlling variable in determining the level of tsunami hazard in corresponding parts of coastlines. This controlling effect is reflected by the relatively smaller hazard in southwest Luzon (between latitude 13° and 15°), which can be explained by the less frequent earthquakes in the source region of zone I. Compared with zone II and zone III, zone I has the lowest seismicity rate, slowest slip rate, and smallest coupling rate, which all lead to the longest earthquake return period in both catalogs. The return period for earthquakes in zone I is 5–10 times as long as for earthquakes with the same magnitude in zone II and zone III for catalog-SB and 2–3 times as long for catalog-GB (Table 1).

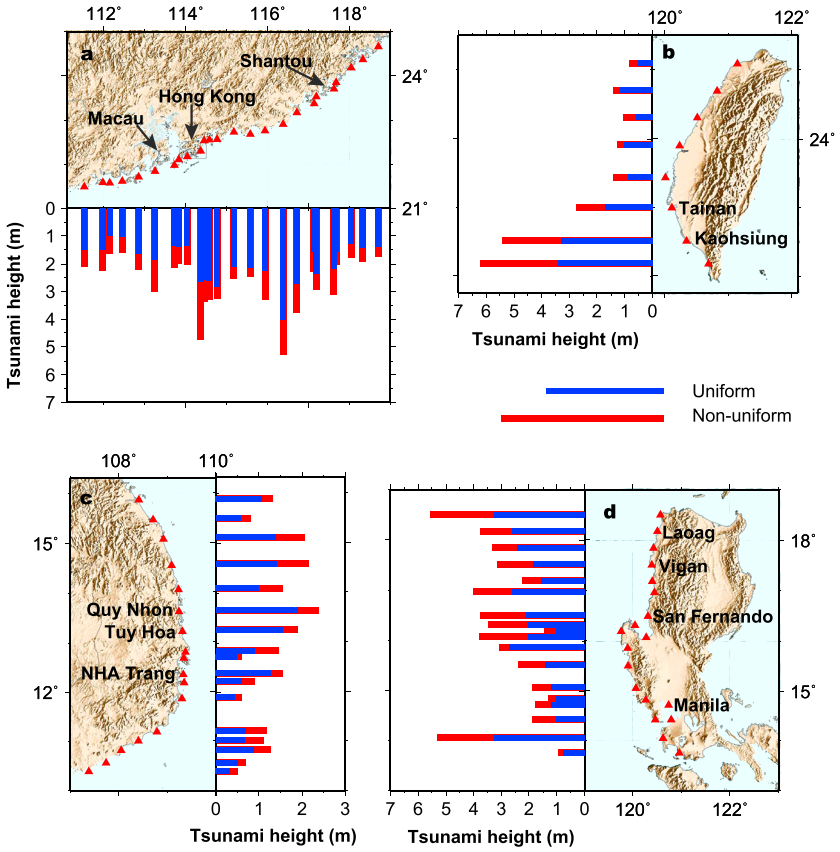

Figure 7. Comparison of expected peak nearshore tsunami amplitude (PNTA) with 1000 year average return period given by approaches based on uniform slip fault model (blue bars) and nonuniform slip fault model (red bars) in (a) southeast China, (b) western Taiwan, (c) central Vietnam, and (d) western Luzon.

5. Effect of Rupture Complexity

To investigate the influence of nonuniform slip distribution pattern on the hazard assessment result, we recalculate all the synthetic earthquakes in both catalogs by replacing nonuniform slip distribution with uniform slip distribution. By keeping the rupture area and fault geometry the same with their nonuniform counterpart, we derive another set of synthetic results. We compare the difference between the results given by uniform slip and nonuniform slip in the form of commonly used hazard expressions. Such expressions include hazard maps of the expected PNTA with specified return periods and hazard curves for locations of interests. We then investigate the statistics of PNTA to explain how the results from nonuniform slip models differ.

Figure 6 compares expected PNTAs in a 500 year return period which are predicted by uniform slip (blue bars) and nonuniform slip model (red bars) along four representative coastlines: southern China, western Taiwan, eastern Vietnam, and western Luzon (for comparison in the whole South China Sea region, readers can refer to Figure S3 for the hazard maps with 100 year, 500 year, and 1000 year return periods). To explain the difference between the results of the uniform slip and nonuniform slip models in another quantitive way, we see the nonuniform slip model predicts 20–60% larger wave amplitudes than the uniform slip model for a 500 year return period, with the average percentages being 35% for west Luzon, 35% for southeast China, and 40%, for east Vietnam (Figure 6). The increase in wave amplitudes for these three regions further rise to 55%, 39%, and 41% on average for a 1000 year return period, with the maximum reaching 86% (corresponding to ~3 m wave height difference, see Figure 7). Comparison of hazard curves for six example locations shows that the divergence between the curves (Figure 8) given by the uniform slip and nonuniform slip models is expanding with the increase in the return period, suggesting that the effect of nonuniform slip is more significant for longer return periods.

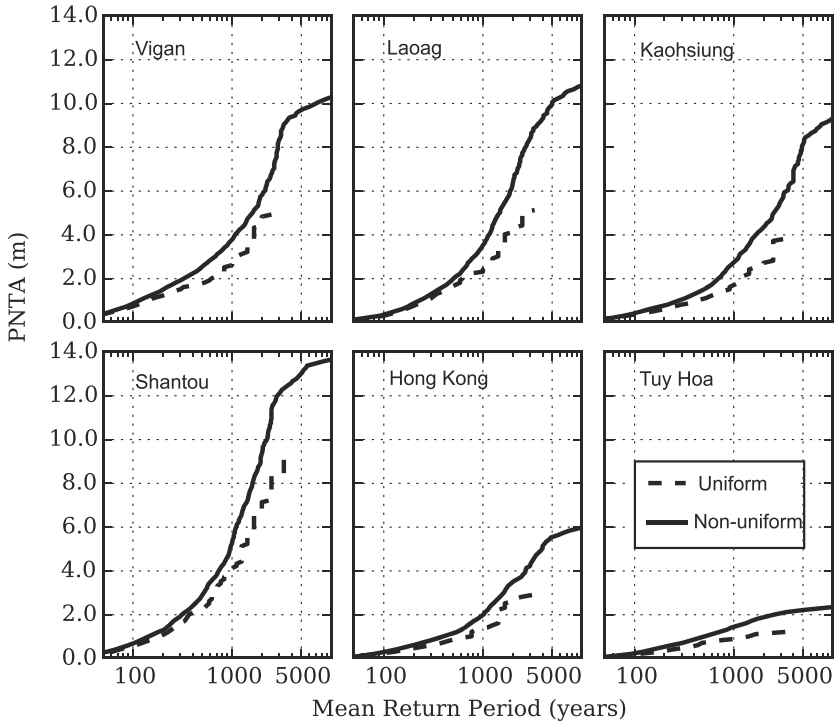

Figure 8. Comparison of hazard curves for six locations of interests, from near-source to far-field locations. Solid lines indicate the result predicted by nonuniform slip. Dashed lines indicate the result predicted by uniform slip models.

The underprediction by uniform slip models is significant when considered in terms of future risk assessment, inundation evaluation, or land use planning. Let us take risk assessment as an example and look at fragility curves developed in Japan, Indonesia, Thailand, and American Samoa-USA [*Mas et al*., 2012]. If we consider one of the most important components of such assessment—building damage probability, we can observe that damage probability increases rapidly (from 0 to 0.6–0.9, depending on building material, such as wood, stone/brick/concrete block, or reinforced concrete) as the inundation depth increases from 0 to 4 m. The rapid increase in damage probability for the first 4 m of inundation depth implies that a 1–2 m increase at this range may lead to as large as a 30%–70% higher probability of building damage at the same location. As such, the much larger damage probability predicted by the nonuniform slip model suggests that the uniform slip model significantly underpredicts the potential economic loss. One thing we must keep in mind is that the 1–2 m difference of PNTA is at depths of 10 m. When a tsunami propagates onshore, its wave height could be amplified several times due to shoaling effects. Then, the 1–2 m difference could in fact be much larger, leading to dramatically different inundation characteristics.

The effect of nonuniform slip is not only significant in the near-source locations as shown by previous studies [e.g., *Geist*, 2002; *Geist and Dmowska*, 1999]. Unexpectedly, such effects are also very significant relatively far field, e.g., in SE China and central Vietnam. This raises the question of at which distance from the rupture area should we still take the effect of slip distribution patterns into account. If this effect is not considered, then to what extent might we underestimate the potential hazard? The nonnegligible effect of nonuniform slip put on SE China and east Vietnam obviously challenges the commonly accepted opinion that the details of slip distribution have very limited effect on far-field tsunami amplitude [*Okal*, 1988]. In both SE China and east Vietnam coast, the hazard level predicted after considering the effect of slip complexity is clearly significantly larger than the one based on the commonly used uniform slip method, although these two regions could be defined as far-field according to the definitions given by NOAA (National Oceanic and Atmospheric Administration) in which regions having 1000 km travel distance or larger than 2 h traveltime are far-field (east Vietnam is $>$ 1000 km away from the Manila Trench, and tsunami wave traveltime from the trench to SE China is longer than 3.5 h, see the definition in http://nthmp-history.pmel.noaa.gov/terms.html). When compared with other ocean basins, the South China Sea is a much smaller and confined region with the area of only 1/50 of the Pacific Ocean and 1/20 of the Indian Ocean, while our definition of far-field tsunamis is

presumably based on the scale of the Pacific Ocean, where ~60% of tsunamis occurred according to historical data [*Gusiakov*, 2009]. In the case of smaller seas, like the South China Sea, the Mediterranean Sea, and the Caribbean Sea, the far-field definition is likely not appropriate. Our study demonstrates that slip complexity has a strong influence even when the propagation distance is around 1000 km (for east Vietnam, the distance is 1000–1300 km), or the traveltime is longer than 2 h (for southeast China, the tsunami travel is 3–4 h). This information is important for future tsunami hazard assessment. It applies to both the probabilistic-based approach and the scenario-based approach that slip complexity should be taken into account not only in the near-field but also in the relative far-field of regional seas which have similar sizes to the SCS. Distance and tsunami traveltime, of course, are not the only factors determining the significance of such an effect. Another factor is whether the receiving coastline is directly exposed to the tsunami path, which in turn is strongly affected by source directivity and irregularity of bathymetry along the wave propagation path [*Okal*, 2008]. However, in practice, source directivity and bathymetry irregularity can be predicted in advance if plate tectonics and bathymetric data are known.

To understand why the nonuniform models generate higher tsunami hazard probabilities than the uniform slip models, we can, for example, take M_w 8.0 events and plot their generated PNTAs along the coasts of five selected regions, namely, west Luzon, south east China, central Vietnam, north Borneo, and east Malaysia (Figure 9). These M_w 8.0 events are chosen from catalog-SB, which consists of 230 events in 100,000 years duration. Comparison of PNTA distribution between nonuniform and uniform events clearly shows that nonuniform events generate on average larger tsunami waves (the red and blue lines represent the mean values for the nonuniform models and the uniform models, respectively) and have a broader wave height coverage, especially in the near-source region. For example, in west Luzon, the maximum and minimum PNTAs differ on average by a factor of ~10 for uniform slip events and ~22 for nonuniform slip events. The effect of nonuniform slip distribution weakens from near field to far field. Compared with the mean PNTAs generated by uniform slip events, the mean PNTAs generated by nonuniform slip events are 47% higher in west Luzon, 37% higher in SE China, 35% higher in central Vietnam, 24% higher in north Borneo, and 27% higher in east Malaysia. In contrast to previous studies on the effect of heterogeneous slip distribution in which the fault rupture areas are fixed for all the slip models, thus only one uniform slip model needs to be considered for comparison [e.g., *Geist*, 2002; *Mueller et al*., 2015], in our study, the rupture area of each earthquake event is randomly selected in the specified fault geometry. The randomly selected rupture area which may span from southern offshore Taiwan to western offshore Palawan is the major contributor to the variability of PNTAs generated by uniform slip events. Additionally, if randomly selected rupture areas are combined with randomly generated slip distributions, the variability of PNTAs generated by nonuniform slip events further increases. Histograms of PNTA distributions of nonuniform events display much more pronounced skewness with a long tail toward larger wave heights than the PNTA distributions of uniform events (Figure 10), again implying that using uniform slip models in PTHA underestimates the potential tsunami hazard. Last but not least, the PNTA distribution patterns exemplified for M_w 8.0 earthquakes can also be observed for earthquakes with other magnitudes (see Figure S4 for the PNTA distributions given by M_w 8.2, M_w 8.4 earthquakes using southern China as an example region).

6. Discussion

6.1. Adequacy of Earthquake Numbers

One important question to be addressed in such Monte Carlo-type analysis is whether a specific number of simulated events can adequately capture the potential tsunami wave height range. The challenge of answering this question in this study is, unlike in previous studies in which normally only one single earthquake magnitude with a fixed rupture area is investigated [*Fukutani et al*., 2014; *Geist*, 2002; *McCloskey et al*., 2007], that we examine varied earthquake magnitudes with numerous randomly chosen rupture areas. For each chosen offshore location, the variability of its PNTAs would be caused by both the variations in rupture areas and the variations in slip distribution patterns. Figure 11 shows the coefficient of variation (COV) of PNTAs at six selected locations as a function of the number of model runs. Three curves in subfigures represent M_w 8.0 (black), M_w 8.4 (red), and M_w 8.8 (blue). Notably, for earthquake magnitudes $<$8.0, more model runs are needed ($>$100 for Vigan, Laoag, and Kaohsiung) than the runs for earthquake magnitudes $>$8.8 ($<$50 for Vigan, Laoag, and Kaohsiung) to reach a stabilized COV. The required number of model runs for M_w 8.4

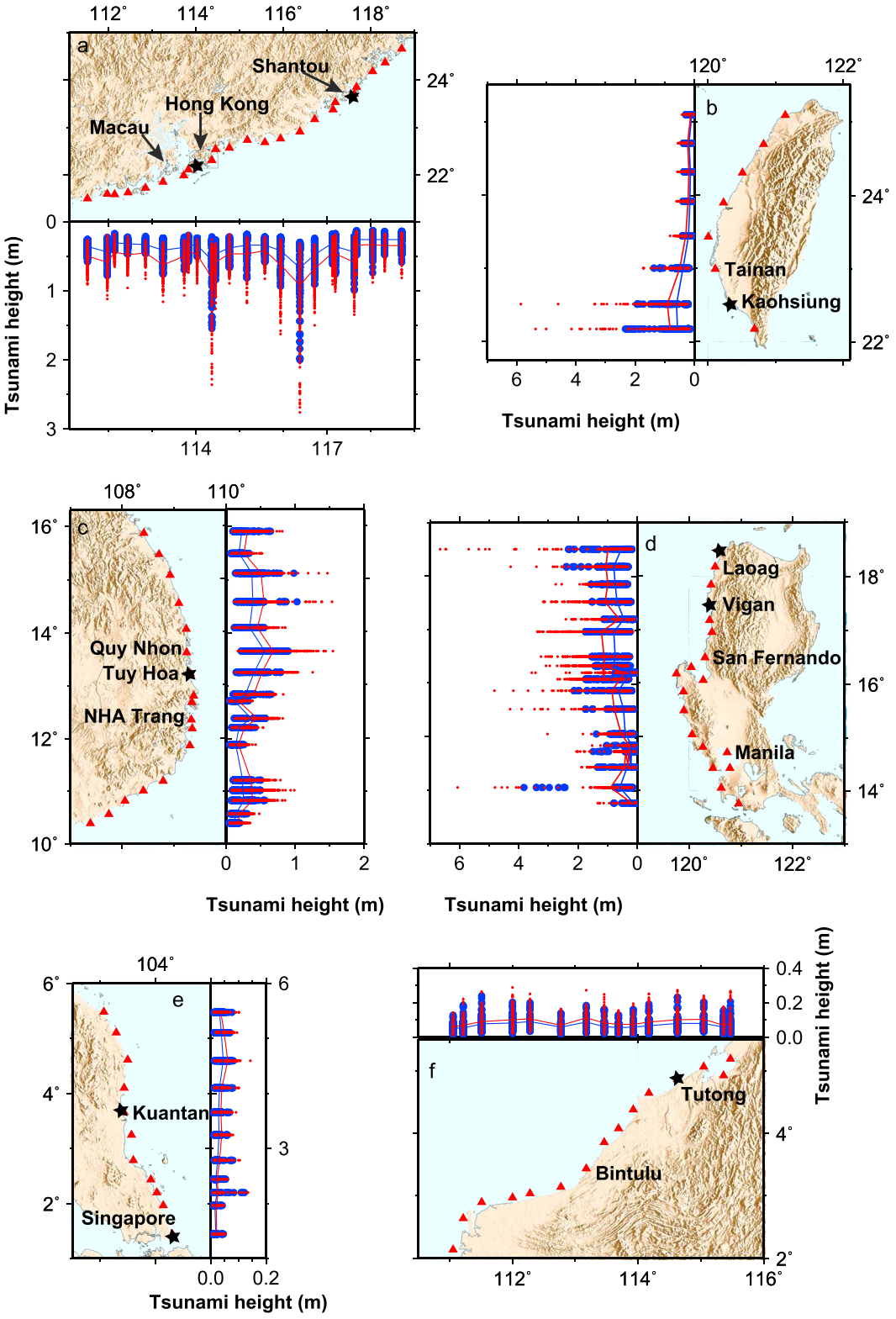

Figure 9. Peak nearshore tsunami amplitude distribution generated by 230 M_w 8.0 synthetic earthquakes along the coast of (a) Southeast China, (b) western Taiwan, (c) central Vietnam, (d) western Luzon, (e) eastern Malaysia, and (f) North Borneo. Red dots represent the PNTAs by earthquakes with nonuniform slip. Blue dots represent the PNTAs by earthquakes with uniform slip. Red lines and blue lines connect the mean PNTAs at each SWGs, corresponding to nonuniform slip and uniform slip, respectively.

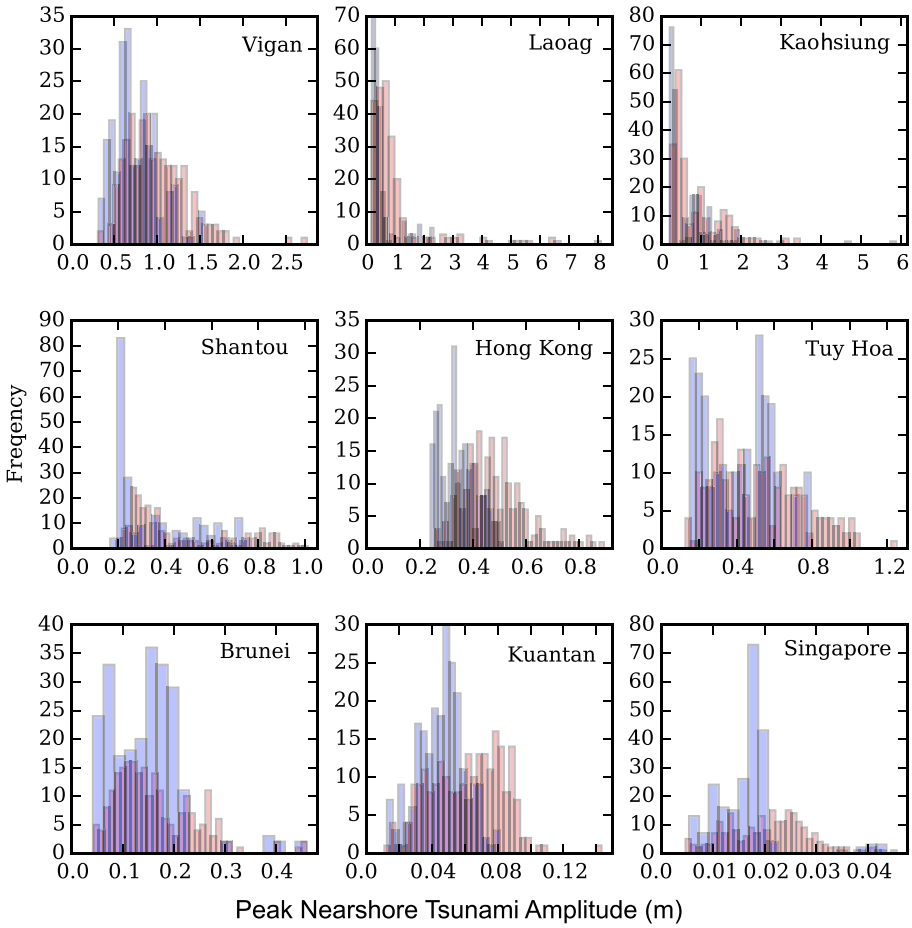

Figure 10. Histogram comparison of PNTAs generated by 230 M_w 8.0 synthetic earthquakes at nine selected locations (see black stars for these locations in Figure 9). Red bars represent histogram of nonuniform slip model. Blue bars are uniform slip model.

earthquakes is between 50 and 100. We can understand this trend by looking at the two main variation contributors: the possible rupture area and the slip distribution pattern. For earthquakes smaller than or equal to M_w 8.4, the rupture area could be anywhere in the three zones we defined. However, increased magnitudes increase also the size of the rupture area, thus leaving fewer options of where the rupture area could be located. As such, earthquakes larger than M_w 8.4 only occur in zone III and have a relatively fixed rupture area. The limits on the location of the rupture area for larger magnitude earthquakes suggests that as the earthquake magnitudes grow, variability in slip distribution patterns becomes the main contributor to PNTAs. Another general trend is apparent when we compare the number of required model runs for locations in the near-source regions (e.g., Vigan, Laoag, and Kaohsiung) with the relatively far-field regions (e.g., Shantou, Hong Kong, and Nha Trang). Here we can see locations in the relative far field require fewer model runs to reach a stabilized COV. This makes sense since the longer traveling distance makes the PNTAs less sensitive to different slip distribution patterns. The first trend that larger earthquakes require smaller number of synthetic events is in our favor as earthquake numbers included in synthetic catalogs show the same decreasing trend (determined by the longer return period, larger earthquakes have a smaller number of events in each synthetic catalog, see supporting information Table S1). Presumably, the second trend that far-field locations require fewer model runs to capture the variation in PNTAs allows us to address the adequacy question by only looking at whether the number of events included in the catalog exceeds the number of model runs required for the examined earthquake magnitude in the near-source locations. By comparing the number of model runs required and the number of events included in the catalogs for each earthquake magnitude at two near-source locations—Kaohsiung and Laoag (Figure S5), we show that synthetic catalogs

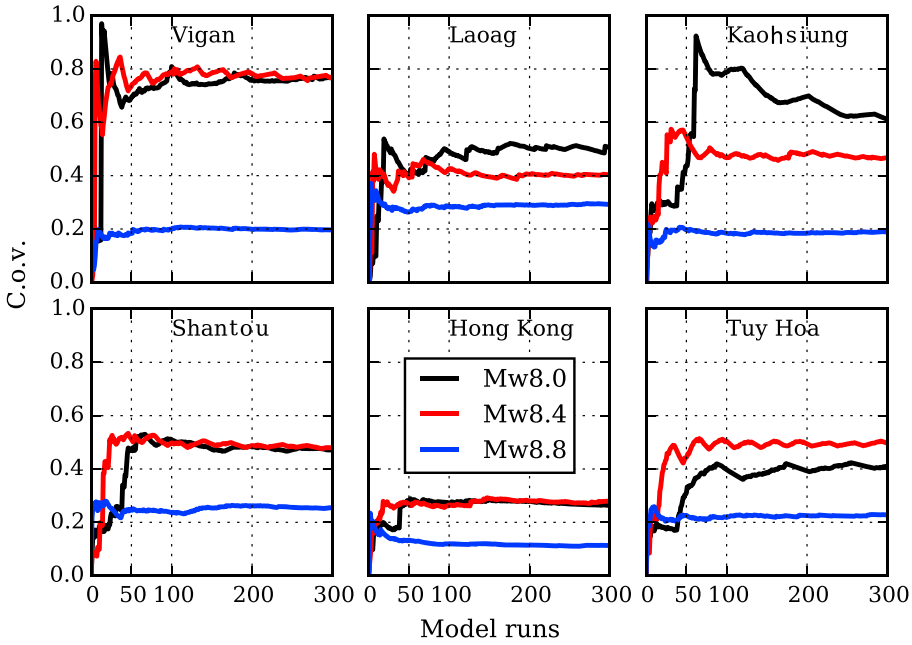

Figure 11. Coefficient of variation for PNTAs at six representative locations as a function of the number of synthetic model runs for earthquakes with magnitude M_w 8.0 (black lines), M_w 8.4 (red lines), and M_w 8.8 (blue lines).

with 100,000 years' duration are, in general, long enough to represent and capture the natural variability of PNTAs in this study.

6.2. Effect of Patch Size

There is a compromise when we choose the average size of unit patches. On the one hand, the size of each patch should be sufficiently large to avoid dispersion effects which will be more significant if initial wavelength is too small or the propagation distance is too long [*Grilli et al*., 2013; *Saito et al*., 2014]. On the other hand, the patch size should be small enough to capture the details of heterogeneous seafloor deformation. It is worth to mention that COMCOT does not account for dispersion in the governing equations. In this study, our intention is to find the most appropriate approximate patch size to avoid dispersion effect rather than simulate it. To determine the patch size which would be large enough to allow us to ignore the dispersion effect, we use the criterion introduced by *Kajiura* [1963]: $(6h/R)^{1/3}(a/h) > 4$, where R is the propagation distance and α is the dominant width of the tsunami source. Assuming an average seafloor depth h of 3 km for the SCS, we see that the required patch size largely depends on the propagation distance. For regions very close to the source (e.g., $<$ 10 km), patch size around 10 km is acceptable, while for longer propagation distances (e.g., $>$1000 km), a larger patch size is required (~45 km). To adequately approximate the seafloor displacement field, previous studies [*Geist*, 2002; *Geist and Dmowska*, 1999] show that the recommended patch size should be less than or equal to the source depth. As the source depth varies from 5 km to 45 km in our case, it means varied patch sizes could be chosen depending on how deep the subduction zone earthquake is. For an earthquake as shallow as 3–25 km in depth (with 14° dip angle), previous numerical experiments [*Geist*, 2002] show a 10 km patch size is small enough to reproduce the local nearshore tsunami amplitude. Based on all the aforementioned constraints put on the patch size, we understand it is very difficult to determine a unified patch size which is small enough to represent the seafloor displacement (~10 km), yet large enough to neglect dispersion effects during propagation (~45 km) at the same time.

To better constrain how the choice of patch size affects the probabilistic hazard assessment, besides the current results based on 20 km patch size, we ran additional two sets of numerical experiments using average patch sizes of 10 km and 40 km. Following the same modeling scheme (see section 2), two sets of Green's function are calculated with finer and coarser patch sizes, respectively. Nonuniform slip distribution patterns are generated based on the newly predefined rupture areas. The nonuniform slip distribution models were then applied to all the synthetic earthquakes ($M_w \geq 7.0$) with 10 km patch size and applied only to larger

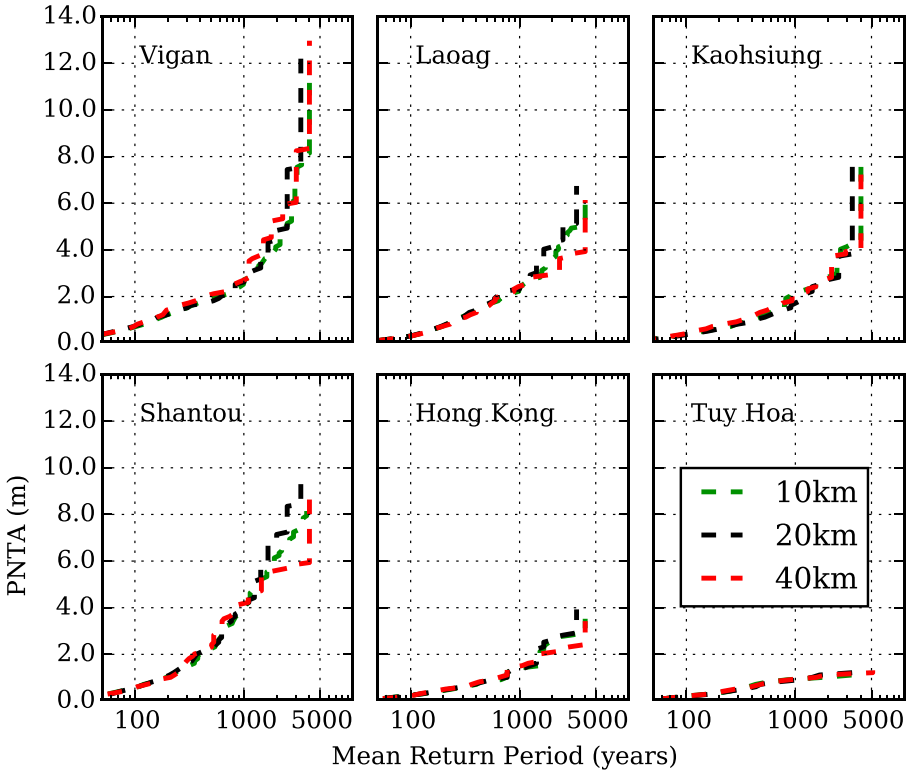

Figure 12. Comparison of hazard curves calculated by three different patch sizes with uniform slip distribution: 10 km (green dashed lines), 20 km (black dashed lines), and 40 km (red dashed lines).

earthquakes ($M_w \geq 8.4$) with 40 km patch sizes (nonuniform slip distribution can only be applied when there is a sufficient number of patches in the dip and strike directions; e.g., for a 10 km patch size, an M_w 7.0 earthquake contains 4×4 patches, while for a 40 km patch size, it only contains 1×1). Corresponding to the uniform slip result for a 20 km patch, we also acquire the uniform slip result for a 10 km patch and a 40 km patch. Thus far, we have six sets of results: three of which are based on the uniform slip model, and the other three are based on the nonuniform slip model.

We first compare the results based on the uniform slip model. The results using three different patch sizes produce almost identical hazard curves, especially for a return period shorter than 1000 years (see Figure 12 for a comparison of expected PNTAs as a function of the return period at six selected locations calculated by using 10 km, 20 km, and 40 km patches). We observe a negligible difference between these hazard curves for both near-source locations (e.g., Vigan) and relatively far-field locations (e.g., Tuy Hoa, for a comparison of more locations, Figure S6 gives expected PNTAs in the next 1000 years among three patch sizes). Although at some locations (e.g., Shantou), results using a 40 km patch give a slightly lower wave height when the return period is long (>3000 years), the difference, in general, is not significant. The insignificant difference among the results based on different patch sizes suggests that the dispersion effect induced by using a smaller patch size could be ignored in this study area. This finding improves our understanding of the patch size effect on the condition of nonuniform slip model. We can attribute the difference between the results produced by different patch sizes to their ability of resolving slip distribution rather than dispersion effect.

We then compare the other three sets of results based on the nonuniform slip models. Figure 13 gives the comparison of expected PNTAs in a 500 year return period along the coast of south China, west Taiwan, east Vietnam, and west Luzon. We can see that the difference induced by using different patch sizes is very pronounced for the near-source locations (southwest Taiwan and west Luzon), especially between PNTAs given by 10 km and 40 km patches (e.g., the 10 km patch gives 66% higher PNTAs than the 40 km patch in southern Taiwan). Compared with PNTAs given by the 10 km patch, the PNTAs produced by the 20 km patch are very close (less than 0.2 m difference) at most locations, except in few near-trench locations (e.g., Kaohsiung in the

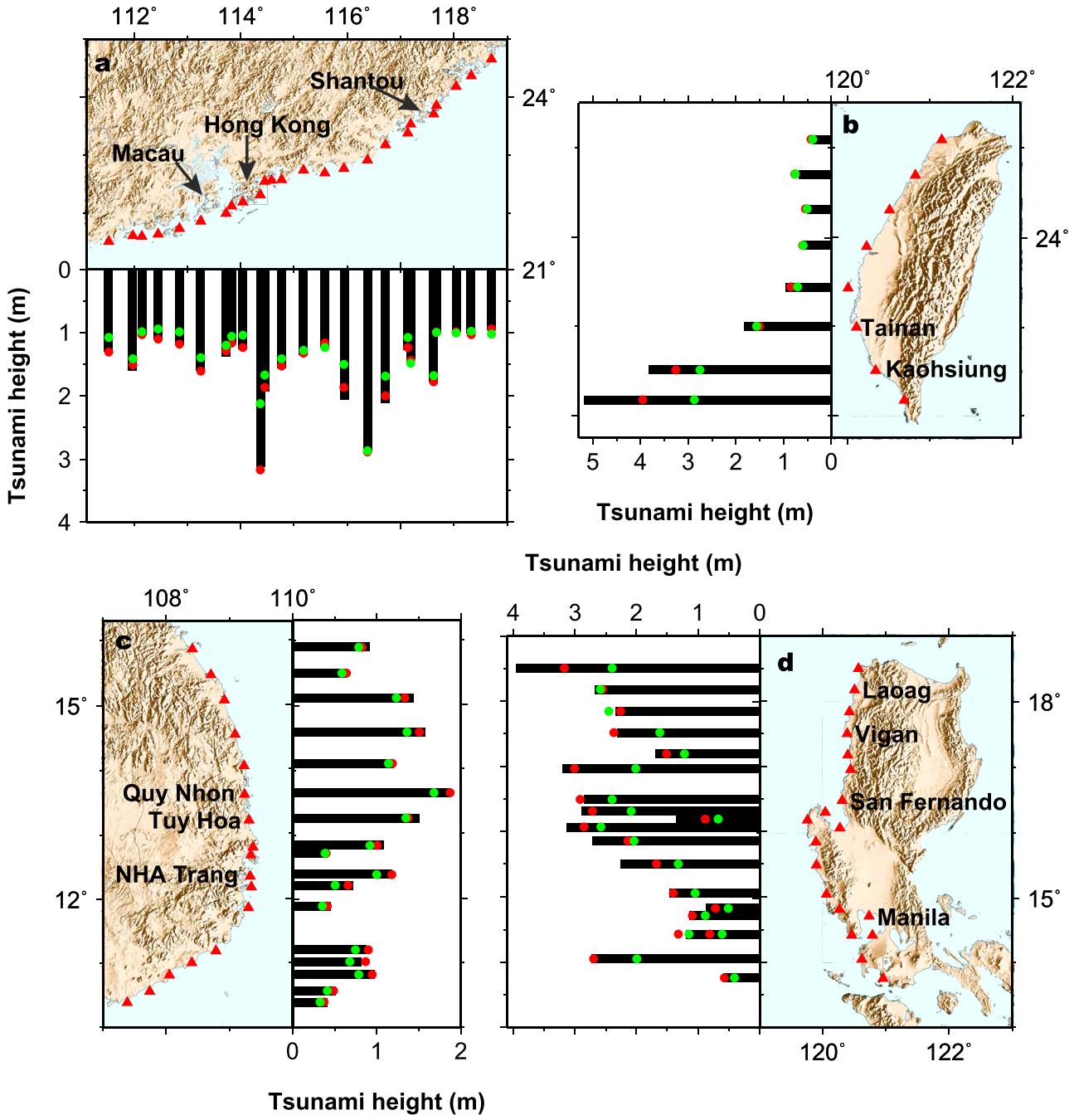

Figure 13. Expected wave height in a 500 year return period given by three different patch sizes: 10 km (black bars), 20 km (red dots), and 40 km (green dots) at offshore region of (a) southeast China, (b) western Taiwan, (c) central Vietnam, and (d) western Luzon.

southwest Taiwan). However, the PNTAs given by the 40 km patch is significantly lower (the calculated heights are ~60–70% of the value given by the 10 km patch) in most of the near-source locations. Similarly, the significant underestimation in the near-source field by using the 40 km patch is also observed in the comparison of expected PNTAs for a 1000 year return period (Figure S7). The comparison between the hazard curves of selected locations shows that the discrepancy between the results given by the different patch sizes increases with the increased time frame (Figure 14). The increased discrepancy is a product of the increased time frame as the increased time frame means larger magnitude earthquakes are included and the asperities of larger earthquakes are the primary sources of discrepancy. Again, this trend is more

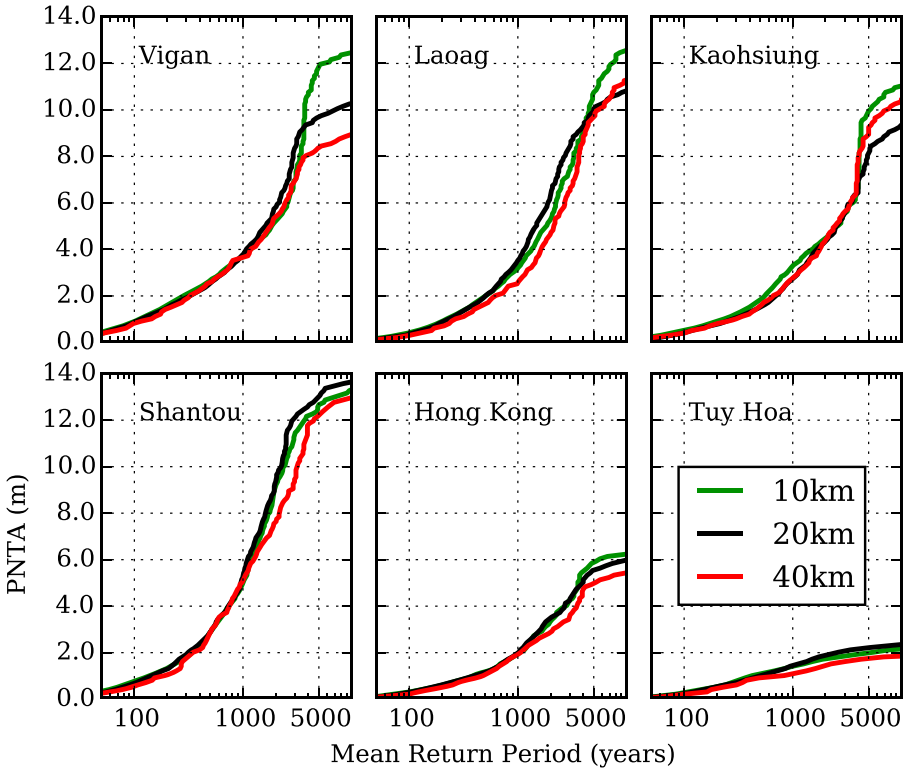

Figure 14. Comparison of hazard curves calculated by three different patch sizes with nonuniform slip distribution: 10 km (green solid lines), 20 km (black solid lines), and 40 km (red solid lines).

pronounced in the near-source locations (e.g., west Luzon), and the underestimation by the 40 km patch becomes nonnegligible for longer return periods (>2000 years) for locations in SE China (e.g., Shantou).

To summarize the patch effect on hazard assessment, we can observe a general trend that smaller patch sizes give relatively larger wave heights than larger patch sizes at the majority of (Figure 13 and S7) locations. This trend is presumably due to smaller patch sizes being able to capture higher gradients of the slip distribution, which could not be resolved by larger patch sizes. However, the difference is only significant for the near-source locations. The comparison of hazard maps and hazard curves suggests that choosing a suitable patch size mainly depends on the distance of the locations of interest from the source region: for the near-source region, a 40 km patch is obviously too large for such a PTHA study if we intend to incorporate the effect of different slip patterns. Although smaller patch sizes are preferred in order to capture the details of slip distribution, one practical issue is that using smaller patch sizes significantly increases the computational load (for the probabilistic calculation in this study, the time required for 10 km, 20 km, and 40 km patches is 21 days, 5 days, 6 h, respectively). The dramatically increased calculation time causes Green's Function approach to lose its advantage of being efficient. In this case study, a 20 km patch therefore becomes an ideal choice that provides acceptable accuracy, negligible dispersion effect, and a reasonable computation time.

6.3. Effect of Fault Geometry

We also consider the uncertainty in fault geometry by constructing the other three fault geometries based on previously published studies [*Megawati et al.*, 2009], earthquake focal mechanisms, and an ideal planar assumption with a constant dip angle of 17.9° (see the 3-D fault geometries in Figure S8a–8d). A comparison of hazard curves in nine representative locations (Figure S9) shows that the PTHA results are not very sensitive to the fault geometries. The discrepancy between PNTAs estimated by different geometries is almost identical in most locations. A considerable difference appears only in Vigan and Shantou when long return periods (>2000 years) are concerned. The negligible difference caused by these fault geometries indicates that using different fault geometries does not affect the conclusions we draw about the effect of the heterogeneous slip model.

7. Conclusions and Implications

Using the SCS as a case study, we have shown that assuming a uniform slip distribution for all the synthetic events in PTHA will greatly underestimate the hazard level not only in the near-source region but also in the relatively far-field regions. In the SCS, PTHA considering the effect of nonuniform slip predicts a 20–60% larger wave amplitude than PTHA based on uniform slip models for a 500 year return period and 20–86% larger for a 1000 year return period. The increased average percentages are 55% in west Luzon, 39% in southeast China, and in east Vietnam 41% for a 1000 year return period. The demonstration that the effect of nonuniform slip is still significant in southeast China and east Vietnam suggests such an effect should also be taken into account in PTHA for other regional seas with similar or smaller size and for regions in the big oceans but not far from tsunamigenic subduction zones. This suggestion also applies to scenario-based tsunami hazard assessment for which only limited numbers of scenarios (most with uniform slip distributions) are simulated. Such estimates might be extremely dangerous since their results can only represent few possible cases, mostly with underestimated hazard, among countless possibilities.

To better capture rupture complexity, a sufficiently small patch size is required. However, the choice of patch size is also determined by the distance of the target coastline from the source and constrained by dispersion effect during wave propagation and by computational costs. As demonstrated in this study, a 10 km patch size is preferred for the near-source region, e.g., west Luzon, and a 40 km patch is acceptable for southeast China and east Vietnam. The requirement for a small patch size in the near-source region raises an important question about one of the main components in any tsunami warning system: the precomputed tsunami unit source function database. The database allows a quick forecast of tsunami wave heights using a linear combination of selected unit sources [*Greenslade et al*., 2014; *Morrissey*, 2011; *Tang et al*., 2009; *Titov et al*., 2005]. With the idea that too large patch size may underestimate the potential tsunami hazard in the near-source region in mind, we can see that the size of a "unit source" used in most of the current tsunami warning systems (e.g., 100×50 km in the Pacific Tsunami warning system [*Tang et al*., 2009] and the Indian tsunami warning system [*Greenslade et al*., 2014]) might be too large to forecast tsunami wave heights and inundation accurately. For those tsunami-prone coastlines close to large subduction zones, precomputed databases with finer unit sources are recommended. However, such improved accuracy can only be achieved if reliable coseismic slip distribution models can be acquired quickly, which in turn relies heavily on the coverage of real-time seismic, geodetic, and tsunami data [*Gusman et al*., 2014; *Melgar et al*., 2013].

It is worth to mention that although the three-zone model we used in this study does not include large earthquakes that could rupture through zone II, we do acknowledge the possibility that the rupture-across-zone earthquake could occur along the Manila Trench. Such "unexpected" events did occur in other subduction zone previously. Examples include the 2011 Tohoku-oki earthquake rupturing through large segments of the Japan trench [*Koyama et al*., 2013], the 1868 Arica earthquake rupturing across the Nazca Ridge [*Okal et al*., 2006], and the 2007 Solomon Islands earthquake rupturing across the triple junction between the Pacific, Australian, and Woodlark Plates [*Taylor et al*., 2008]. Without considering the largest possible earthquake, our model may underestimate the potential hazard level for a very long return period (e.g., $>$2000 years). More comprehensive studies in the future should integrate all the possible sources (e.g., volcanic eruptions, earthquakes, and submarine landslides) and discuss impact of aleatoric and epistemic uncertainties of the source parameters.

Acknowledgments

We highly appreciate the help from Ya-Ju Hsu, who generously shared the MATLAB code for fault geometry and gave us her insightful suggestions when we were developing the Gutenberg-Richter relationships. Great thanks to František Gallovič for sharing his slip generator code (http://fgallovic.github.io/SlipGen/) and helpful discussion on code function. We also thank Eric L. Geist and Christof Mueller for their valuable review comments. This research is supported by the National Research Foundation Singapore under its Singapore NRF Fellowship scheme (National Research Fellow Award NRF-RF2010-04) and administered by the Earth Observatory of Singapore, the National Research Foundation Singapore, and the Singapore Ministry of Education under the Research Centres of Excellence initiative. Robert Weiss was partially supported by NSF-CMMI-1208147 and NSF-CMMI-1206271 for this work. The bathymetric data used in this study are downloaded from http://www.gebco.net.

References

Ader, T., et al. (2012), Convergence rate across the Nepal Himalaya and interseismic coupling on the Main Himalayan Thrust: Implications for seismic hazard, *J. Geophys. Res.*, *117*, B04403, doi:10.1029/2011JB009071.

Ammon, C. J., et al. (2005), Rupture process of the 2004 Sumatra-Andaman earthquake, *Science*, *308*(5725), 1133–1139.

Annaka, T., K. Satake, T. Sakakiyama, K. Yanagisawa, and N. Shuto (2007), Logic-tree approach for probabilistic tsunami hazard analysis and its applications to the Japanese coasts, *Pure Appl.Geophys.*, *164*(2–3), 577–592.

Bautista, M. L. P., B. C. Bautista, J. C. Salcedo, and I. C. Narag (2013), Philippine tsunamis and seiches (1589–2012), *A Catalogue of Tsunami Events in the Philippines*, Philippine Institute of Volcanol. and Seismol., Diliman, Quezon City.

Blaser, L., F. Krüger, M. Ohrnberger, and F. Scherbaum (2010), Scaling relations of earthquake source parameter estimates with special focus on subduction environment, *Bull. Seismol. Soc. Am.*, *100*(6), 2914–2926, doi:10.1785/0120100111.

Burbidge, D., P. R. Cummins, R. Mleczko, and H. K. Thio (2008), A probabilistic tsunami hazard assessment for Western Australia, *Pure Appl. Geophys.*, *165*(11–12), 2059–2088.

Cao, J.-H., J.-L. Sun, H.-L. Xu, and S.-H. Xia (2014), Seismological features of the littoral fault zone in the Pearl River Estuary, *Chin. J. Geophys.*, *57*(2), 498–508, doi:10.6038/cjg20140215.

Dao, M. H., P. Tkalich, E. S. Chan, and K. Megawati (2009), Tsunami propagation scenarios in the South China Sea, *J. Asian Earth Sci.*, *36*(1), 67–73, doi:10.1016/j.jseaes.2008.09.009.

Fukutani, Y., A. Suppasri, and F. Imamura (2014), Stochastic analysis and uncertainty assessment of tsunami wave height using a random source parameter model that targets a Tohoku-type earthquake fault, *Stoch. Environ. Res. Risk Assess.*, 1–17, doi:10.1007/s00477-014-0966-4.

Gallovič, F., and J. Brokešová (2004a), The k^{-2} rupture model parametric study: Example of the 1999 Athens earthquake, *Stud. Geophys. Geod.*, *48*(3), 589–613, doi:10.1023/B:SGEG.0000037473.70906.08.

Gallovič, F., and J. Brokešová (2004b), On strong ground motion synthesis with k^{-2} slip distributions, *J. Seismol.*, *8*(2), 211–224, doi:10.1023/B:JOSE.0000021438.79877.58.

Gallovič, F., and J. Brokešová (2007), Hybrid *k*-squared source model for strong ground motion simulations: Introduction, *Phys. Earth Planet. Inter.*, *160*(1), 34–50, doi:10.1016/j.pepi.2006.09.002.

Geist, E. L. (1998), Local tsunamis and earthquake source parameters, *Adv. Geophys.*, *39*, 117–209.

Geist, E. L. (2002), Complex earthquake rupture and local tsunamis, *J. Geophys. Res.*, *107*(5), 2086, doi:10.1029/2000JB000139.

Geist, E. L., and R. Dmowska (1999), Local tsunamis and distributed slip at the source, *Pure Appl.Geophys.*, *154*(3–4), 485–512.

Greenslade, D. J. M., et al. (2014), An assessment of the diversity in scenario-based tsunami forecasts for the Indian Ocean, *Cont. Shelf Res.*, *79*, 36–45.

Grilli, S. T., J. C. Harris, T. S. Tajalli-Bakhsh, T. L. Masterlark, C. Kyriakopoulos, J. T. Kirby, and F. Shi (2013), Numerical simulation of the 2011 Tohoku tsunami based on a new transient FEM co-seismic source: Comparison to far-and near-field observations, *Pure Appl.Geophys.*, *170*, 1333–1359.

Gusiakov, V. K. (2009), Tsunami history: Recorded, in *The Sea*, edited by E. N. Bernard and A. R. Robinson, Harvard Univ. Press, Cambridge, Mass.

Gusman, A. R., Y. Tanioka, B. T. MacInnes, and H. Tsushima (2014), A methodology for near-field tsunami inundation forecasting: Application to the 2011 Tohoku tsunami, *J. Geophys. Res. Solid Earth*, *119*, 8186–8206, doi:10.1002/2014JB010958.

Hartzell, S. H., and T. H. Heaton (1983), Inversion of strong ground motion and teleseismic waveform data for the fault rupture history of the 1979 Imperial Valley, California, earthquake, *Bull. Seismol. Soc. Am.*, *73*(6A), 1553–1583.

Herrero, A., and P. Bernard (1994), A kinematic self-similar rupture process for earthquakes, *Bull. Seismol. Soc. Am.*, *84*(4), 1216–1228.

Hsu, Y. J., S.-B. Yu, J. Loveless, T. Bacolcol, J. Woessner, and R. Solidum (2015), Interseismic deformation and moment deficit along the Manila subduction zone and the Philippine Fault system, *AGU Fall Meeting 2015, Abstract S33A-2747*, San Francisco.

Hsu, Y.-J., S.-B. Yu, T.-R. A. Song, and T. Bacolcol (2012), Plate coupling along the Manila subduction zone between Taiwan and northern Luzon, *J. Asian Earth Sci.*, *51*, 98–108, doi:10.1016/j.jseaes.2012.01.005.

Johnson, J. M., and K. Satake (1994), Rupture extent of the 1938 Alaskan earthquake as inferred from tsunami waveforms, *Geophys. Res. Lett.*, *21*(8), 733–736, doi:10.1029/94GL00333.

Kajiura, K. (1963), The leading wave of a tsunami, *Bull. Earthquake Res. Inst. Tokyo*, *41*(3), 531–571.

Koyama, J., K. Yoshizawa, K. Yomogida, and M. Tsuzuki (2013), Variability of megathrust earthquakes in the world revealed by the 2011 Tohoku-oki Earthquake, *Earth Planets Space*, *64*(12), 1189–1198, doi:10.5047/eps.2012.04.011.

Lau, A. Y. A., A. D. Switzer, D. Dominey-Howes, J. C. Aitchison, and Y. Zong (2010), Written records of historical tsunamis in the northeastern South China Sea—Challenges associated with developing a new integrated database, *Nat. Hazards Earth Syst. Sci.*, *10*(9), 1793–1806, doi:10.5194/nhess-10-1793-2010.

Li, L., A. D. Switzer, Y. Wang, R. Weiss, Q. Qiu, C.-H. Chan, and P. Tapponnier (2015), What caused the mysterious eighteenth century tsunami that struck the southwest Taiwan coast?, *Geophys. Res. Lett.*, *42*, 8498–8506, doi:10.1002/2015GL065567.

Liu, P. L. F., S. B. Woo, and Y. S. Cho (1998), Computer programs for tsunami propagation and inundation *Rep.*, Cornell Univ. Ithaca, New York.

Liu, P. L. F., X. Wang, and A. J. Salisbury (2009), Tsunami hazard and early warning system in South China Sea, *J. Asian Earth Sci.*, *36*(1), 2–12, doi:10.1016/j.jseaes.2008.12.010.

Liu, Y., A. Santos, S. M. Wang, Y. Shi, H. Liu, and D. A. Yuen (2007), Tsunami hazards along Chinese coast from potential earthquakes in South China Sea, *Phys. Earth Planet. Inter.*, *163*(1–4), 233–244, doi:10.1016/j.pepi.2007.02.012.

Løvholt, F., G. Pedersen, S. Bazin, D. Kühn, R. E. Bredesen, and C. Harbitz (2012), Stochastic analysis of tsunami runup due to heterogeneous coseismic slip and dispersion, *J. Geophys. Res.*, *117*, C03047, doi:10.1029/2011JC007616.

Mas, E., S. Koshimura, A. Suppasri, M. Matsuoka, M. Matsuyama, T. Yoshii, C. Jimenez, F. Yamazaki, and F. Imamura (2012), Developing Tsunami fragility curves using remote sensing and survey data of the 2010 Chilean Tsunami in Dichato, *Nat. Hazards Earth Syst. Sci.*, *12*(8), 2689–2697.

McCaffrey, R. (2008), Global frequency of magnitude 9 earthquakes, *Geology*, *36*(3), 263–266, doi:10.1130/g24402a.1.

McCloskey, J., A. Antonioli, A. Piatanesi, K. Sieh, S. Steacy, S. S. Nalbant, M. Cocco, C. Giunchi, J. D. Huang, and P. Dunlop (2007), Near-field propagation of tsunamis from megathrust earthquakes, *Geophys. Res. Lett.*, *34*, L14316, doi:10.1029/2007GL030494.

McCloskey, J., A. Antonioli, A. Piatanesi, K. Sieh, S. Steacy, S. Nalbant, M. Cocco, C. Giunchi, J. Huang, and P. Dunlop (2008), Tsunami threat in the Indian Ocean from a future megathrust earthquake west of Sumatra, *Earth Planet. Sci. Lett.*, *265*(1–2), 61–81, doi:10.1016/j.epsl.2007.09.034.

Megawati, K., F. Shaw, K. Sieh, Z. Huang, T.-R. Wu, Y. Lin, S. K. Tan, and T.-C. Pan (2009), Tsunami hazard from the subduction megathrust of the South China Sea: Part I. Source characterization and the resulting tsunami, *J. Asian Earth Sci.*, *36*(1), 13–20.

Melgar, D., B. W. Crowell, Y. Bock, and J. S. Haase (2013), Rapid modeling of the 2011 M_w 9.0 Tohoku-oki earthquake with seismogeodesy, *Geophys. Res. Lett.*, *40*, 2963–2968, doi:10.1002/grl.50590.

Morrissey, W. A. (2011), Tsunamis: Monitoring, detection, and early warning systems, in *Tsunamis: Causes, Characteristics, Warnings and Protectionon*, edited by N. Veitch and G. Jaffray, pp. 215–224, Nova Sci., New York.

Mueller, C., W. Power, S. Fraser, and X. Wang (2015), Effects of rupture complexity on local tsunami inundation: Implications for probabilistic tsunami hazard assessment by example, *J. Geophys. Res. Solid Earth*, *120*, 488–502, doi:10.1002/2014JB011301.

Mueller, C., J. Mountjoy, W. Power, E. Lane, and X. Wang (2016), Towards a spatial probabilistic submarine landslide hazard model for submarine canyons, in *Submarine Mass Movements and Their Consequences*, edited by G. Lamarche et al., pp. 589–597, Springer, Cham, doi:10.1007/978-3-319-20979-1_59.

Okada, Y. (1985), Surface deformation due to shear and tensile faults in a half-space, *Bull. Seismol. Soc. Am.*, *75*, 1135–1154.

Okal, E. A. (1988), Seismic parameters controlling far-field tsunami amplitudes: A review, *Nat. Hazards*, *1*(1), 67–96.

Okal, E. A. (2008), Excitation of tsunamis by earthquakes, in *The Sea: Ideas and Observations on Progress in the Study of the Seas*, vol. 15, edited by E. N. Bernard and A. R. Robinson, pp. 137–177, Harvard Univ. Press, Cambridge.

Okal, E. A., J. C. Borrero, and C. E. Synolakis (2006), Evaluation of tsunami risk from regional earthquakes at Pisco, Peru, *Bull. Seismol. Soc. Am.*, *96*(5), 1634–1648, doi:10.1785/0120050158.

Okal, E. A., C. E. Synolakis, and N. Kalligeris (2011), Tsunami simulations for regional sources in the South China and adjoining seas, *Pure Appl. Geophys.*, *168*(6–7), 1153–1173.

Papazachos, B. C., E. M. Scordilis, D. G. Panagiotopoulos, C. B. Papazachos, and G. F. Karakaisis (2004), Global relations between seismic fault parameters and moment magnitude of earthquakes, *Bull. Seismol. Soc. Greece*, *XXXVI*, 1482–1489.

Paris, R., A. Switzer, M. Belousova, A. Belousov, B. Ontowirjo, P. Whelley, and M. Ulvrova (2014), Volcanic tsunami: A review of source mechanisms, past events and hazards in Southeast Asia (Indonesia, Philippines, Papua New Guinea), *Nat. Hazards*, *70*(1), 447–470.

Power, W., X. Wang, E. Lane, and P. Gillibrand (2013), A probabilistic tsunami hazard study of the auckland region. Part I: Propagation modelling and tsunami hazard assessment at the shoreline, *Pure Appl. Geophys.*, *170*(9–10), 1621–1634.

Ren, Y., R. Wen, and Y. Song (2014), Recent progress of tsunami hazard mitigation in China, *Episodes*, *37*(4), 277–283.

Rhie, J., D. Dreger, R. Bürgmann, and B. Romanowicz (2007), Slip of the 2004 Sumatra-Andaman earthquake from joint inversion of long-period global seismic waveforms and GPS static offsets, *Bull. Seismol. Soc. Am.*, *97*(1 A SUPPL), S115–S127.

Saito, T., D. Inazu, T. Miyoshi, and R. Hino (2014), Dispersion and nonlinear effects in the 2011 Tohoku-Oki earthquake tsunami, *J. Geophys. Res. Oceans*, *119*, 5160–5180, doi:10.1002/2014JC009971.

Satake, K. (1987), Inversion of tsunami waveforms for the estimation of a fault heterogeneity: Method and numerical experiments, *J. Phys. Earth*, *35*, 241–254.

Satake, K. (1989), Inversion of tsunami waveforms for the estimation of heterogeneous fault motion of large submarine earthquakes: The 1968 Tokachi-oki and 1983 Japan Sea earthquakes, *J. Geophys. Res.*, *94*(B5), 5627–5636, doi:10.1029/JB094iB05p05627.

Satake, K., Y. Fujii, T. Harada, and Y. Namegaya (2013), Time and space distribution of coseismic slip of the 2011 Tohoku earthquake as inferred from tsunami waveform data, *Bull. Seismol. Soc. Am.*, *103*(2B), 1473–1492, doi:10.1785/0120120122.

Sieh, K., D. H. Natawidjaja, A. J. Meltzner, C. C. Shen, H. Cheng, K. S. Li, B. W. Suwargadi, J. Galetzka, B. Philibosian, and R. L. Edwards (2008), Earthquake supercycles inferred from sea-level changes recorded in the corals of west Sumatra, *Science*, *322*(5908), 1674–1678.

Somerville, P., K. Irikura, R. Graves, S. Sawada, D. Wald, N. Abrahamson, Y. Iwasaki, T. Kagawa, N. Smith, and A. Kowada (1999), Characterizing crustal earthquake slip models for the prediction of strong ground motion, *Seismol. Res. Lett.*, *70*(1), 59–80, doi:10.1785/gssrl.70.1.59.

Sørensen, M. B., M. Spada, A. Babeyko, S. Wiemer, and G. Grünthal (2012), Probabilistic tsunami hazard in the Mediterranean Sea, *J. Geophys. Res.*, *117*, B01305, doi:10.1029/2010JB008169.

Tang, L., V. V. Titov, and C. D. Chamberlin (2009), Development, testing, and applications of site-specific tsunami inundation models for real-time forecasting, *J. Geophys. Res.*, *114*, C12025, doi:10.1029/2009JC005476.

Taylor, F. W., R. W. Briggs, C. Frohlich, A. Brown, M. Hornbach, A. K. Papabatu, A. J. Meltzner, and D. Billy (2008), Rupture across arc segment and plate boundaries in the 1 April 2007 Solomons earthquake, *Nat. Geosci.*, *1*(4), 253–257. [Available at http://www.nature.com/ngeo/journal/v1/n4/suppinfo/ngeo159_S1.html.]

Thio, H. K., P. Somerville, and G. Ichinose (2007), Probabilistic analysis of strong ground motion and tsunami hazards in southeast Asia, *J. Earthquake Tsunami*, *01*(02), 119–137, doi:10.1142/S1793431107000080.

Titov, V. V., F. I. González, E. N. Bernard, M. C. Eble, H. O. Mofjeld, J. C. Newman, and A. J. Venturato (2005), Real-time tsunami forecasting: Challenges and solutions, in *Developing Tsunami-Resilient Communities: The National Tsunami Hazard Mitigation Program*, edited by E. N. Bernard, pp. 41–58, Springer, Dordrecht, Netherlands, doi:10.1007/1-4020-3607-8_3.

Wang, K., and S. L. Bilek (2014), Invited review paper: Fault creep caused by subduction of rough seafloor relief, *Tectonophysics*, *610*, 1–24, doi:10.1016/j.tecto.2013.11.024.

Wang, X. (2009), User manual for COrnell Multi-grid COupled Tsunami model-COMCOT V1.7, edited. [Available at http://ceeserver.cee.cornell.edu/pll-group/doc/COMCOT_User_Manual_v1_7.pdf.]

Wu, T.-R., and H.-C. Huang (2009), Modeling tsunami hazards from Manila trench to Taiwan, *J. Asian Earth Sci.*, *36*(1), 21–28, doi:10.1016/j.jseaes.2008.12.006.

Yue, H., and T. Lay (2013), Source rupture models for the M_w 9.0 2011 Tohoku earthquake from joint inversions of high-rate geodetic and seismic data, *Bull. Seismol. Soc. Am.*, *103*(2B), 1242–1255, doi:10.1785/0120120119.